

IGHMBP2 deletion suppresses translation and activates the ISR

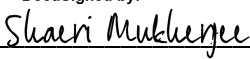
by
Jesslyn Park

DISSERTATION
Submitted in partial satisfaction of the requirements for degree of
DOCTOR OF PHILOSOPHY

in
Biochemistry and Molecular Biology

in the
GRADUATE DIVISION
of the
UNIVERSITY OF CALIFORNIA, SAN FRANCISCO

Approved:

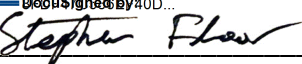
DocuSigned by:

7AA908684B40471... Shaeri Mukherjee
Chair

DocuSigned by:

DocuSigned by:4DC... Sophie Dumont

DocuSigned by:

DocuSigned by:740D... Kevan M. Shokat

DocuSigned by:

3709C3C6AF93461... Stephen Floor

Committee Members

Copyright 2023

by

Jesslyn Park

Acknowledgements

Intellectual liberation through education motivated my pursuit of graduate study, and I owe thanks to many who contributed toward surpassing this milestone. I thank my thesis committee for their academic guidance: my advisor Stephen Floor, my chair Shaeri Mukherjee, Sophie Dumont, and Kevan Shokat. My scientific growth was served by their interdisciplinary perspectives, advice, and encouragement. Stephen shows trainees great faith in their potential and motivates exploration, learning, and collaboration. I am grateful for my training in the Floor lab, where I also worked alongside wonderful labmates who taught me so much. I especially wish to acknowledge those who directly aided my project—Hetvee, José, Sohyun, Ziad, and Albert—who I have gained enormously from working with. I also thank Srivats Venkataramanan, Jess Sheu-Gruttadauria, and Yizhu Lin for their guiding wisdom throughout my time in the lab.

Several other members of the UCSF community supported my graduate experience in various ways. I am thankful for friendships found in my Tetrad cohort, support from our program manager, Toni Hurley, whenever needed, and the empowerment and advocacy I have received from D’Anne Duncan, Alece Alderson, Tiffany Lam, the First Generation to College organization, and the FG2C student leadership community at UCSF.

Throughout my studies, my growth as a human was bettered, sustained, and championed by incredibly wise, tremendous friends and confidants. Harold, José (also the most supportive labmate I could ask for), Pranav, Zara, Lindsey, Alain—thank you for giving me courage, and coincidentally also being my scientific & personal role models—

and also Kayleigh, Dianne, Evelyn, Ben, Elisabeth, Conrad, Kelsey, Dan, Brittney, Ranya, Linda, Fred, Lisa, Nick. I am privileged to have been surrounded by such special and kind people who I admire and appreciate deeply. The times we spent outside the lab, and especially their support near the challenging final stretch—the baked good drop-offs, hangouts over games, catching shows and concerts, inviting cross-overs between groups, commiserating and hearing each other—really kept me going.

To my relatives – my aunt & uncle; Jong Tae & Carol; my brothers; my parents Mei Rong Chen & Hae Gon Park, thank you for being my family. I inherited the resilience I needed to arrive here from my parents especially. To my partner’s relatives, especially Bijal, Jayesh, Nidhi, and Devansh, thank you for your warm support. Finally, I celebrate my partner, Yash, from whom I have received so much these past several years (including some more great friends I also wish to acknowledge—Austin, Don, Sam, Joe, Catherine, Steven, Nate, Daniel, Ian, Carolyn, both Matts, Art, Emma, Claire, Khalid, Emily—thank you for all our shared times). I never used to understand the expression to be one’s rock; I thought it a fairly unappealing and cliché metaphor, other alternatives considered. But I get it now. More eloquently—yet still unoriginal—I shall cite a metaphor used by my favorite writer, Isabel Wilkerson, who had described her partner *a gift from the Universe*. I feel this everyday.

Contributions

Chapter 1 is a background and overview of IGHMBP2 research to-date.

Chapter 2 directly corresponds to the Abstract, adapted from the manuscript pre-print:

IGHMBP2 deletion suppresses translation and activates the integrated stress response. Jesslyn Park, Hetvee Desai, José Liboy-Lugo, Sohyun Gu, Ziad Jowhar, Albert Xu, and Stephen N. Floor. 2023. *bioRxiv* doi: 2023.12.11.571166

To view updated findings from this dissertation, please refer to any subsequent corresponding or peer-reviewed version of our manuscript when available.

IGHMBP2 deletion suppresses translation and activates the integrated stress response

Jesslyn Park

Abstract

IGHMBP2 is a non-essential, superfamily 1 DNA/RNA helicase that is mutated in patients with rare neuromuscular diseases SMARD1 and CMT2S. IGHMBP2 is implicated in translational and transcriptional regulation via biochemical association with ribosomal proteins, pre-rRNA processing factors, and tRNA-related species. To uncover the cellular consequences of perturbing IGHMBP2, we generated full and partial IGHMBP2 deletion K562 cell lines. Using polysome profiling and a nascent protein synthesis assay, we found that IGHMBP2 deletion modestly reduces global translation. We performed Ribo-seq and RNA-seq and identified diverse gene expression changes due to IGHMBP2 deletion, including ATF4 upregulation. With recent studies showing the ISR can contribute to tRNA metabolism-linked neuropathies, we asked whether perturbing IGHMBP2 promotes ISR activation. We generated ATF4 reporter cell lines and found IGHMBP2 knockout cells demonstrate basal, chronic ISR activation. Our work expands upon the impact of IGHMBP2 in translation and elucidates molecular mechanisms that may link mutant IGHMBP2 to severe clinical phenotypes.

Table of Contents

Chapter 1. Background of IGHMBP2	1
1.1 Discovery of IGHMBP2	1
1.2 IGHMBP2 in Disease	3
1.2.a Overview of Spinal Muscular Atrophy with Respiratory Distress Type 1	3
1.2.b Overview of Charcot-Marie-Tooth Disease	4
1.2.c Polymorphism of IGHMBP2 in SMARD1 versus CMT2S	5
1.3 Experimental Background of IGHMBP2	6
1.3.a Genetic and biochemical characterization of IGHMBP2	6
1.3.b Overview of IGHMBP2 in model systems	8
1.3.b.i IGHMBP2 in yeast	8
1.3.b.ii IGHMBP2 in mice	9
1.3.b.iii IGHMBP2 in mouse cells	10
1.3.b.iv IGHMBP2 in human cells	11
1.4 Thesis Project Outlook	12
Chapter 2. IGHMBP2 suppresses translation and activates the integrated stress response	13
2.1 Introduction	13
2.2 Results	15
2.2.a IGHMBP2 deletion impacts cellular proliferation and global translation ..	15
2.2.b Ribosome profiling reveals differentially expressed genes in IGHMBP2 deletion cells	17

2.2.c ATF4 is upregulated in IGHMBP2 deletion cells	19
2.2.d IGHMBP2 deletion results in ISR activation	20
2.3 Discussion.....	22
2.4 Materials & Methods	26
2.5 Competing Interest Statement.....	36
2.6 Acknowledgements & Author Contributions.....	36
References	58

List of Figures

Figures	38
Figure 1. IGHMBP2 deletion decreases proliferation of cells.....	38
Figure 2. IGHMBP2 deletion reduces global translation in cells.	39
Figure 3. IGHMBP2 loss alters translation of diverse mRNAs.	40
Figure 4. ATF4 is upregulated in IGHMBP2 deletion cells.	41
Figure 5. The ISR is activated in IGHMBP2 deletion cells.	42
Supplemental Figures	43
Figure S1. IGHMBP2 deletion clone genotyping and characterization.	46
Figure S2. Nascent polypeptide synthesis assay with parental versus IGHMBP2 deletion clones.	47
Figure S3. RNA-seq and Ribo-seq count correlation between replicate samples.	48
Figure S4. Periodicity profiles of Ribo-seq samples.....	49
Figure S5. Strand sense analysis among Ribo-seq reads.	50
Figure S6. Read-mapping classifications of Ribo-seq samples.	51
Figure S7. Translational efficiency of ATF4 is differentially upregulated in IGHMBP2 deletion cells.	52
Figure S8. ATF4 reporter cell line characterization.	53
Figure S9. Differential p-eIF2 α levels at steady-state in IGHMBP2 deletion clones is not detected by Western blot.....	54
Figure S10. Ribosome footprint analyses across transcript regions and codons.	55
Figure S11. GSEA with ATF4 target gene list.....	56

List of Tables

Tables	57
Supplemental Table A. Prelim. functional assessment of IGHMBP2 mutagenesis ...	57
Supplemental Table 1. RNA-seq and Ribo-seq DEG results lists.	57
Supplemental Table 2. RNA-seq and Ribo-seq GSEA results lists.	57

Glossary

Biological Terminology

DNA - deoxyribonucleic acid; encodes instructions for all genes, resides in the nucleus as a double-stranded molecule made of nucleotides (DNA sequence)

RNA - ribonucleic acid; transcribed from DNA, is processed and exported into the cytoplasm as a single-stranded molecule made of nucleotides (RNA sequence), may form bonds among single strand as secondary structures

helicase - enzyme that unwinds DNA and/or RNA to make accessible for other processes, as DNA/RNA can form secondary structures that require “unzipping”

SF1 - Superfamily 1; family of helicases, encompasses IGHMBP2

genotype - genetic/sequence characteristic

phenotype - trait/observable characteristic

codon - RNA code made of 3 nucleotides that translate to a particular amino acid (carried by tRNAs that contain a specific **anticodon** sequence to correspond to/ “decode” codons on mRNA), or instruct to START/STOP translation

DNA mutagenesis - when DNA sequence is changed, causing genetic variation (**polymorphism**) which may cause downstream changes to translated amino acid (**missense**) & may or may not change protein function, or create a new STOP codon (**nonsense**) causing a **truncated** protein, or shift (**frameshift**) the rest of the code which may cause significant sequence changes, or may result in no change to the amino acid sequence (**silent**), as amino acids are redundantly encoded by multiple **codons**

indel - insertion-deletion in genomic DNA sequence, mutagenesis event during DNA repair, may disrupt protein expression as a functional **knockout/deletion**

transcription - production of RNA by protein machinery that “reads” DNA as template

translation - production of proteins (functional, folded **polypeptides**) by ribosomes that “read” messenger RNA (mRNA) as template, active polypeptide synthesis is also referred to as **elongation**

transcriptome - all RNA transcripts present in the cell (variable across different cells or conditions)

translatome - all active translation processes in the cell (variable across different cells or conditions)

proteome - all proteins that have been synthesized in the cell (variable across different cells or conditions)

PCR - polymerase chain reaction, a method to generate copies (clone; amplify) of DNA for downstream use and detectability (**qPCR** as a method for quantification of specific sequences)

UTR - untranslated region of mRNA, upstream (5'UTR) or downstream (3'UTR) of the coding sequence (CDS) which encodes protein, may contain regulatory elements that influence translation

DEG - differentially expressed gene via change to its transcription or translation, and thus exhibiting different mRNA and/or protein levels

TE - translation efficiency rate via ribosomes per gene (see 2.2.b)

K562; K-562 - immortalized lymphoblast (**hemopoietic/blood cell type**) cell line derived from bone marrow of female leukemia patient; triploid karyotype

CRISPR-Cas9 - gene-editing machinery derived from prokaryotic genes involving clustered regularly interspaced short palindromic repeats; CRISPR-associated enzyme 9 (Cas9) has been engineered to be readily targeted/“guided” to a particular DNA sequence in the genome by complexing it to a single guide RNA (sgRNA) specific to the genomic region of interest. Cas9 then cuts and breaks the targeted DNA, triggering DNA repair mechanisms, which can result in an **indel** event. More specific editing may be achieved by supplying repair DNA sequences for use as a template by DNA repair machinery.

CRISPRi - CRISPR interference, gene-editing machinery where Cas9 has been engineered not to cut DNA (deactivated, known as dCas9) and also fused with a transcriptional repressor (KRAB domain in our **K562 CRISPRi cell line**), therefore typically targeted near the transcriptional start site of genes (**promoter** region) to block transcription without the need for DNA breakage

endogenous - inherent to the biological system, may reflect basal/homeostatic/ steady-state conditions

transgene; transgenic - containing gene artificially introduced from another source (**exogenous**)

non-essential gene - deletion of the gene is not lethal to cell/organism

fitness gene - non-essential gene, yet reduces fitness when deleted

ISR - integrated stress response, cellular pathway to respond to stress (see 2.2.d)

Genes

ATF4 - Activating transcription factor 4, up-regulates ISR-response genes

eIF2 α - ekaryotic initiation factor 2 α (subunit 1), its phosphorylated state (p-eIF2 α)
disrupts translation and promotes ISR activation

GCN2 - kinase that phosphorylates eIF2 α when stalled ribosomes are sensed

IGHMBP2 - Immunoglobulin heavy chain (μ) binding protein 2; human helicase

Subp-2 - the homologue (version) of IGHMBP2 gene in mice

ribosome; 80S; 60S; 40S - translation machinery comprised of ribosomal proteins and ribosomal RNAs (**rRNA**); 'S' denotes Svedberg's unit/sedimentation coefficient corresponding to relative densities; during translation initiation, the 40S **subunit** scans mRNA until encountering a START codon, is joined by 60S, and the 80S ribosome (**monosome**) is formed; when multiple ribosomes are engaged to a transcript, these complexes are referred to as **polysomes**

tRNA - transfer RNA, carries amino acids to transfer to polypeptides being synthesized at the ribosomal **A-site** (aminoacyl); **isodecoders** are individual tRNA variants of unique sequences; isodecoders with the same anticodon (see **codon**) are grouped as **isoacceptors**; isoacceptors that carry the same amino acid are grouped as an **isotype**. The human genome encodes more than 400 unique tRNAs corresponding to only 21 amino acids (including selenocysteine) and thus isodecoder diversity may contribute to translation regulation

Clinical Terminology

CMT2S - Charcot-Marie-Tooth disease Type 2 subtype S (see 1.2.b)

SMARD1 - spinal muscular atrophy with respiratory distress type 1 (see 1.2.a)

motoneuron; motor neuron - transmits signals from brain or spinal cord to muscle

muscular atrophy - decline/degeneration of muscles tissues

myopathy; myopathic - disease that impacts muscle tissue

neural - any type of nerve tissue cell (neurons/**neuronal**, or other brain cells; glia)

neurodegeneration - degeneration, loss, and/or damage to neural cells

neurogenic - caused by or originating from nervous system

neuromuscular - intersection between neural and muscular function

nmd - neuromscular degeneration, abbreviation for IGHMBP2-disrupted model mice

peripheral neuropathy - disease afflicting nerves outside of the brain/spinal cord

Experimental Methods

Flow cytometry - method to measure fluorescent signals emitted by individual cells
(form of “single-cell” analysis)

Northern blot - visualize RNA abundance, usually using nucleic acid probes that can hybridize (bind) to RNA of interest, which can then be chemically attached to some marker enabling detection

Western blot - visualize protein abundance, usually using antibodies specific to protein of interest, which can then be chemically attached to some marker

enabling detection. “Western” (and “**Northern**”) is a spin-off name from Southern blot (DNA detection), named after Edwin Southern

OPP assay - O-propargyl-puromycin is an analog of puromycin, which resembles tRNA_{Tyr} and is thus incorporated into polypeptides during translation elongation. OPP can then be chemically “clicked” to a fluorophore as an assay (measure) of active translation (**nascent polypeptide/protein synthesis assay**).

Polysome profiling - experimental method to quantify relative abundance of ribosomal species (40S; 60S; 80S; polysomes) in sample

Ribo-seq; ribosome profiling - experimental method to examine and quantify ribosome-footprint (actively translated) mRNA sequences in sample

RNA-seq - experimental method to examine and quantify RNA sequences (actively transcribed) in sample

Sanger sequencing - low-throughput sequencing strategy that relies on individual sequencing reactions, enabling quantification of single genes of interest

NGS sequencing - high-throughput sequencing strategy that enables numerous DNA sequences to be read in parallel, generating large datasets informing quantitative information corresponding to thousands of genes

Sequencing pre-processing - computational methods to refine raw sequencing data, for example, by trimming unnecessary barcode sequences, filtering sequences (**reads**) that may be too short to specifically match (**map**) to the genome, etc.

Sequencing analysis - computation methods to define how sequencing data is statistically changed between samples. This may reflect, for example, gene

expression changes in response to different stimuli such as stress conditions, disease, drug treatments, or changes inherent to different cell types, among other experimental possibilities; elucidates biological pathways/networks and possibly identifies key genetic changes underlying phenotypic outcomes

GSEA - gene set enrichment analysis; rather than genes at individual level, identifies changes pertaining to a group of functionally-related genes according to differential fold-change rankings across all sequenced genes

Metagene analysis - computational methods to visualize sequence enrichment trends across all reads in sample (“**globally**”); in our case, using Ribo-seq to depict ribosomal footprint occupancy across all transcripts and thus visualize changes that may occur at a specific stage of translation (i.e. initiation, elongation, termination)

Codon enrichment analysis - computational methods typically using ribosome profiling data to determine whether ribosomes are enriched/**stalled** on a particular codon; for example, observing increased frequency of codons corresponding to the ribosomal A-site footprint position may point to the occurrence of empty **A-site** stalling caused by specific tRNA deficiency

Chapter 1.

Background of IGHMBP2

1.1 Discovery of IGHMBP2

Immunoglobulins, also known as antibodies, comprise several classes of heavy chain structures that are interchanged via recombination of different exons at switch regions (Stavnezer et al. 2008). In the early 1990's, a gene in mice was discovered to bind DNA switch regions encoding heavy μ -chains (S_μ), derived from studying a group of spleen cell clones numbered "2" screened for S_μ hybridization activity, and these binding proteins were thus named $S\mu bp-2$ (Mizuta et al. 1993). $S\mu bp-2$ expression was found in diverse tissue types such as thymus and spleen tissues. $S\mu bp-2$ was also determined to encode several helicase motifs corresponding with helicase superfamily 1, as well as a nuclear localization signal (NLS) consistent with its DNA-interaction capabilities. Interestingly, the authors also noted that part of the sequence of $S\mu bp-2$, which lacked most helicase domains, was homologous to human glial factor-1 (GF-1). Discovered a few years prior to transcriptionally regulate neurotropic viral protein JCV B, GF-1 transcripts were observed to be most abundant in brain and kidney tissues from mice, and were also found to progressively increase in abundance in mice brain tissue across development (Kerr & Khalil, 1991).

The full-length human homologue of $S\mu bp-2$, which shares at least 90% sequence conservation with the mouse gene, was soon shown to function similarly via binding assays demonstrating engagement with human and mice S_μ motifs $((GAGCT)_n(GGGCT))_m$ and $((GAGCT)_n(GGGGT))_m$, respectively (Fukita et al. 1993).

Thus, the human homologue of *Sμbp-2* was eventually named immunoglobulin heavy μ -chain switch binding protein 2 (IGHMBP2).

In the mid-late 1990's, researchers at the Jackson Laboratory, a hub for mouse research, identified mice with symptoms of neuromuscular degeneration. This lineage was named *nmd* model mice, and genetic mapping was performed that identified mutated *Sμbp-2* as the cause of disease. However, no clinical records had yet existed linking IGHMBP2 mutations to any human diseases (Cox et al. 1998). Meanwhile, clinicians studying spinal muscular atrophy (SMA), which was known to be caused by *SMN1* mutations, had begun identifying patients phenotypically diagnosed with SMA without possessing disrupted *SMN1* (Rudnik-Schöneborn et al. 1996; Grohmann et al. 1999). By 2001, IGHMBP2 mutagenesis was identified as the cause of spinal muscular atrophy with respiratory distress type 1 (SMARD1), a new disease category created upon identifying the first cohort of patients with IGHMBP2 mutations among other rare clinical distinctions from SMA (Grohmann et al. 2001).

About a decade after IGHMBP2 mutagenesis was linked to SMARD1 etiology, IGHMBP2 mutations were identified in patients with a rare form of Charcot-Marie-Tooth disease—who lacked respiratory symptoms associated with SMARD1—and thus subtype CMT Type 2S was newly established as an IGHMBP2-linked disease variant (Cottenie et al. 2014). These fairly recent IGHMBP2-associated clinical advances have since motivated research to clarify its molecular role, which has remained relatively understudied since early IGH-interaction characterization described. Investigating IGHMBP2 function and cellular consequences of its disruption may contribute

understanding to neuromuscular disease mechanisms and ultimately inform therapeutic strategies.

1.2 IGHMBP2 in Disease

CMT2S and SMARD1 are autosomal, recessive, and inherited peripheral neuropathies. These severe diseases are characterized by varying degrees in loss of peripheral neuron function that lead to sensory loss and neurogenic-based muscular deformities, muscular atrophy, and muscle weakness. SMARD1 is mainly differentiated by impaired respiratory function in addition to shared pathological presentations with CMT2S patients. In humans, SMARD1 or CMT2S symptom onset usually occurs within the first few months or more than 1 year after birth, respectively (Rzepnikowska & Kochanski, 2021). Over the last few decades, biotechnological advances have expanded accessibility of genetic testing and next-generation sequencing, which notably accelerated awareness of IGHMBP2 clinical relevance among numerous other rare diseases genes (Lei et al. 2022). With such advances, historically elusive or difficult-to-diagnose rare diseases such as SMARD1 and CMT2S remain continuously discovered via more frequent identification and comparative studies of genetic determinants.

1.2.a Overview of Spinal Muscular Atrophy with Respiratory Distress Type 1

SMARD1 is a rare form of SMA and also referred to as distal spinal-muscular atrophy 1 (dSMA1), distal hereditary motor neuronopathy type 6, dHMN6/HMN6, or fatal infantile motor neuron disease. SMARD1 causes low birth weight, muscle weakness,

and respiratory failure (Yuan et al. 2017). SMARD1 usually causes death in afflicted patients within approximately 1 year, although there are documented cases of patients surviving into adolescence and adulthood with ventilatory support (Joseph et al. 2009; Pierson et al. 2011; Messina et al. 2012). While disease prevalence remains challenging to estimate accurately due to the severity of SMARD1, SMA is estimated to occur in approximately 1 in 10,000 live births, with approximately 1% of these patients exhibiting diaphragmatic paralysis (Giannini et al. 2006; Sugarman et al. 2012; Mercuri et al. 2020).

1.2.b Overview of Charcot-Marie-Tooth Disease

CMT is one of the most common human neuromuscular diseases, affecting 1 in 2,500 people via disruptions in over 100 genes, causing variable degrees of peripheral neuropathies (Skre, 1974; Lei et al. 2022). The two major types of CMT are Type 1 (more than half of CMT patients) and Type 2 (one third of CMT2 patients), of which several subtypes are differentiated according to phenotypic and/or genetic determinants. Examples of rarer CMT types include autosomal recessive CMT4 and dominant X-linked CMTX, among others (Banchs et al. 2009).

CMT1 and CMT2 patients have largely overlapping symptoms, including distal sensory loss and reduced motor function that tends to spread and/or become more severe over time. The main differentiator between CMT1 versus CMT2 is type of neuronal degeneration caused. CMT1 is autosomal dominant and primarily characterized by demyelination of peripheral neurons. CMT2 is characterized by axon loss in peripheral neurons, and is therefore referred to as axonal CMT (Grohmann et al.

2001, Cottenie et al. 2014). CMT2 subtypes are either autosomal dominant or recessive, and CMT2S is estimated to occur among approximately 5% of CMT2 patients, although the actual number may vary as most CMT2 patients do not have genetic diagnoses (Yuan et al. 2017; Lei et al. 2022).

1.2.c Polymorphism of IGHMBP2 in SMARD1 versus CMT2S

Clinical databases such as gnomAD and ClinVar document diverse pathogenic and nonpathogenic mutational variants across *IGHMBP2* identified via genetic testing. These databases typically do not identify the polymorphism on both alleles from the same patient. To engineer biologically-relevant models, biallelic polymorphic information among a recessive disease context is important to determine, for example, whether mutagenesis upon both alleles should reflect particular constraints. Therefore, interpretation of mutagenic pathogenicity in patients diagnosed with SMARD1 or CMT2S benefits from surveying detailed case studies.

In our initial assessment of clinical literature where mutation information from both alleles per patient were available, we observed that IGHMBP2 was predicted to be truncated for all protein copies in approximately 1/4 of all patients (Supplemental Table A¹). Most SMARD1 and CMT2S patients possess at least one allele where IGHMBP2 is either frame-shifted or has a nonsense mutation via gaining a premature stop codon,

1: Please note that *Supplemental Table A* is included for preliminary and anecdotal purposes only, reflecting a total of 85 documented cases (58 SMARD1 and 27 CMT2S), which are relatively small sample sizes. Thus, statistical and epidemiological inferences should *not* be made without further review, investigation, and expert clinical perspective. Cross-clinical studies cited may also include genotypes from separate references, or may specifically aim to publish newfound and unique mutations, which may skew actual interpretable frequencies of mutation types. We therefore made our best effort to reduce redundancies in this preliminary analysis and emphasize that contributing new findings toward IGHMBP2 polymorphic frequencies is not within the research scope of the thesis overall.

which leads to functional knockout of protein expression. This suggested full loss protein expression via truncations as a viable and clinically-relevant pathogenetic background that could possibly model either disease, and also implicates relevance of partial IGHMBP2 loss among disease-mutation carriers, who are largely healthy and asymptomatic. Patients otherwise express IGHMBP2 with single missense mutations, some of which have been validated to impair DNA/RNA binding, unwinding, and ATP hydrolysis, further attributing pathogenicity to loss-of-function of IGHMBP2 enzymatic activity perhaps moreso than the disrupted functions of other domains (Guenther et al. 2009a; Lim et al. 2012; Saladini et al. 2020).

Recent literature has suggested SMARD1 versus CMT2S may differentially arise dependent on the structural perturbation caused by IGHMBP2 mutagenesis. IGHMBP2 mutations found in SMARD1 patients are more likely to be missense in the helicase domain, while CMT2S-associated IGHMBP2 mutations comprise various possible nonsense or missense mutations (Saladini et al. 2020). While some CMT2S patients were initially found to express truncated IGHMBP2 in fibroblasts and lymphoblastoid cells in greater levels compared to SMARD1 patient samples, further research is needed to establish connection between truncated IGHMBP2 polypeptide abundance and disease severity (Cottenie et al. 2014; Rzepnikowska & Kochanski, 2021).

1.3 Experimental Background of IGHMBP2

1.3.a Genetic and biochemical characterization of IGHMBP2

IGHMBP2 is located on chromosome 11 on band q13.2-q13.4, encoding 15 exons that translate into a 993 amino acid, 109 kDa enzyme (Fukita et al. 1993;

Grohmann et al. 2001; Maystadt et al. 2004). As a Superfamily 1 helicase, IGHMBP2 exhibits non-ring forming, ATP-dependent 5' to 3' unwinding activity on either DNA or RNA. Besides helicase and ATPase domains, IGHMBP2 contains an R3H motif, which binds single-stranded nucleic acids, as well as an NLS and zinc-finger domain (Maystadt et al. 2004). Nucleotide sequence 1528-2635 of *IGHMBP2* are identical to the sequence of the glial cell-specific 45 kDa transcription factor GF-1, which specifically stimulates the promoter of neurotropic virus JCV (Kerr et al. 1991; Fukita et al. 1993; Chen et al. 1997). While early investigation of IGHMBP2 interrogated its DNA-interacting capabilities, IGHMBP2 is predominantly localized in the cytoplasm and may therefore mostly act on RNA substrates. At an organismal level, IGHMBP2 is expressed ubiquitously across all cell types, mostly at low levels (Cox et al. 1998).

Biochemical work strongly implicates IGHMBP2 in translational regulation via interactions with ribosomal proteins, tRNAs, translation initiation factors, and other genes that indirectly affect regulation (Guenther et al. 2009a; de Planell-Saguer et al. 2009). One such example includes the finding that IGHMBP2 interacts with the transcription factor for RNA pol III (TFIIIC), which is responsible for transcribing tRNA among other small RNAs (de Planell-Saguer et al. 2009). Other transcriptional-translational regulatory possibilities have also been suggested upon the finding that IGHMBP2 biochemically associates with Pontin and Reptin, which are required for small nucleolar ribonucleoprotein expression (de Planell-Saguer et al. 2009).

IGHMBP2 has been experimentally confirmed to unwind both DNA and RNA *in vitro* (Guenther et al. 2009a). We note that IGHMBP2 is relatively dissimilar to related Superfamily 1 helicases, most closely sharing only 48% positive sequence identity to

prototypical Superfamily 1 helicase, UPF1, followed by 44% and 39% positive sequence identity with SenX and MOV10, respectively. These helicases are implicated in diverse functions, including nonsense-mediated mRNA decay (UPF1), transcriptional termination (SenX), and miRNA-dependent regulation (MOV10). On dsDNA, IGHMBP2 has been shown to exhibit slower, short-lived unwinding processivity *in vitro* relative to UPF1 (Mizuta et al. 1993; Kanaan et al. 2018). The relative processivity of IGHMBP2 as an RNA helicase is yet to be determined and will be important to clarify especially upon diverse RNA structures. A resolved RNA-bound structure of IGHMBP2 has further evidenced disease mutations disrupt helicase activity (Guenther et al. 2009a; Lim et al. 2012), and future DNA/RNA-IGHMBP2 mechanistic studies are needed to uncover how enzymatic function in contrast to other possible mechanisms may mediate gene expression.

1.3.b Overview of IGHMBP2 in model systems

1.3.b.i *IGHMBP2 in yeast*

A recent study in *Saccharomyces cerevisiae* (Rzepnikowska et al. 2022) sought to characterize consequences of disrupting the yeast homologue of IGHMBP2, Hcs1, which shares 57% similarity to IGHMBP2 helicase domains. Hcs1 deletion was found to sensitize yeast to 4-chlorophenol, yet only amongst most clones in one of the two tested strains. While a rescue experiment exogenously re-introducing Hcs1 in the knockout strains failed to reverse the growth defective phenotype in media with 4-chlorophenol, Hcs1 knock-in was instead found sensitize yeast to 4-chlorophenol, possibly as Hcs1 overexpression is toxic to cells. Hcs1 deletion was then found to cause hypersensitivity

to treatment with cycloheximide, a translational suppressor, which was partially rescued by exogenous expression of IGHMBP2. This yeast model was then used to establish an assay to differentiate deleterious effects of multiple disease mutants via suppressive growth defects. The finding that human IGHMBP2 can partially rescue Hcs1 also suggests conservation of fundamental molecular pathways involving IGHMBP2 between yeast and humans and further supports its role in translation.

1.3.b.ii IGHMBP2 in mice

IGHMBP2-associated diseased model mice were initially obtained by spontaneous mutagenesis events noticed during routine mice breeding, where researchers then generated an *nmd* mouse lineage. Through a series of crossing mouse lines, mutations in *Sμbp-2* were found to cause incorrect splicing and premature translational termination of *Sμbp-2* mRNA (Cook et al. 1995; Cox et al. 1998). More recently, CRISPR-Cas9 mutagenesis has also enabled the generation of SMARD1 and CMT2S model mice and thus may further empower deeper investigation toward how variable organismal phenotypes arise from IGHMBP2 mutations (Smith et al. 2021; Martin et al. 2022).

Various phenotypic and neurobehavioral assays have been conducted to characterize IGHMBP2-associated disease in mice. SMARD1 and CMT2S model mice exhibit reduced body weight and progressive muscular atrophy compared to healthy mice. Physiological assessments demonstrate *nmd* and CMT2S model mice exhibit weaker sensation, muscle strength, and motor function. Axon abundance, motor branch diameters, and neuromuscular junction occupancy are reduced within tissues. Nerve

conduction velocity is also reduced in model mice, which is a test performed to diagnose humans among other indicators such as muscle wasting and reflexive measurements (Banchs et al. 2009; Martin et al. 2022).

As a follow-up to the biochemical finding that IGHMBP2 co-precipitates with tRNA-Tyr, SMARD1 model mice were also rescued when expressing a genetic modifier locus encoding ABT1 and several tRNA genes, as the femoral nerve and axon counts were shown to grow to the size and abundance found in control mice, respectively (Cox et al. 1998; de Planell-Saguer et al. 2009). This further implicated a connection between tRNAs and IGHMBP2 in disease pathology, although ABT1 is also a target of interest as a regulator of pre-rRNA processing. A recent gene therapy study in mice found that introducing self-complementary adeno-associated virus carrying *ABT1* partially rescued SMARD1 mice in some of the physiological assays performed, and thus future work is needed to address whether expressing tRNA genes is sufficient or more effective in rescuing IGHMBP2-deficient models (Vadla et al. 2022).

1.3.b.iii IGHMBP2 in mouse cells

Various studies using model mouse motoneurons have been conducted largely to assess morphological and physiological defects due to IGHMBP2 deletion. Microscopy has also been performed in both mouse and human cells to determine overall cellular localization of IGHMBP2 and its co-localization partners, such as eIF4G2 and rRNA (Grohmann et al 2004; Guenther et al. 2009a; de Planell-Saguer et al. 2009).

A study of translation in IGHMBP2-deficient mouse motoneurons found no significant global translational changes relative to control mice using diverse assays

such as SILAC, FUNCAT, and SUNSET, and reported only mild transcriptomic changes via RNA-seq (Surrey et al. 2018). Localized translation however, as indicated by expression of a translationally-regulated β -actin GFP-3'UTR reporter, was found to be slowed post-photobleaching. Despite this result, Western blot analysis showed no reduction in β -actin between control and diseased motoneurons. This importantly demonstrated the measurable yet small effect size of IGHMBP2 deletion upon translation in neurons and several examples of its experimental challenges. The authors speculated compartment-specific roles may explain experimental difficulty toward discerning translation changes using bulk samples (Surrey et al. 2018). IGHMBP2 deficiency was ultimately found to corresponded with suppression of IMP1 expression via Western blot. IMP1 binds the 3'UTR of β -actin expression and is known to play a role in neurodegeneration, and thus IMP1 down-regulation was proposed as a possible IGHMBP2-associated disease mechanism for further investigation.

1.3.b.iv IGHMBP2 in human cells

A recent study sought to determine if IGHMBP2 influenced nonsense-mediated mRNA decay (NMD) regulation using motoneurons derived from SMARD1 patient-derived fibroblasts, considering its evolutionary proximity with NMD regulator UPF1 (Taiana et al. 2022). A subset of NMD target mRNAs (CARS, SC35, and RPL3) were found more abundant via qPCR in the IGHMBP2-deficient motoneurons. SMARD1 motoneurons were then partially pathologically rescued when treated with an NMD activator. The authors concluded IGHMBP2 loss impairs NMD, proposing dysregulated mRNA transcript accumulation as a possible disease mechanism.

1.4 Thesis Project Outlook

The fundamental and disease-relevant mechanisms by which IGHMBP2 regulates translation are undefined. As SMARD1 and CMT2S are severe neurodegenerative diseases, producing viable model mice is challenging, costly, and may present a difficult background for precise molecular characterization due to downstream effects that fitness defects impose on animal models. A cell-based model may therefore be leveraged to overcome such challenges, especially as immortalized cells are highly proliferative and thus increase experimental throughput, among other advantages.

This thesis project was conceptualized and conducted in the laboratory of Stephen Floor, which focuses in understanding the molecular contributions of various translation-relevant and human disease-associated macromolecules—such as other helicases like DDX3X, among other RNA-interacting proteins—using a combination of biochemical, tissue culture, tool-design implementation, and bioinformatic approaches. In embarking on this project, no other study to our knowledge had yet determined the impact of IGHMBP2 toward mRNA translation in a human cellular model. We were therefore motivated and positioned to use a human cell line to address the following questions as part of this dissertation:

- How does IGHMBP2 impact cellular fitness?
- How does IGHMBP2 impact global translation?
- What are the gene expression changes in IGHMBP2 deletion cells?
- Which genetic changes are specific to full loss of IGHMBP2 and why?

Chapter 2.

IGHMBP2 suppresses translation and activates the integrated stress response

2.1 Introduction

IGHMBP2 is a ubiquitously-expressed, superfamily 1 (SF1) DNA/RNA helicase implicated in the regulation of mRNA translation (Grohmann et al. 2001; de Planell-Saguer et al. 2009). IGHMBP2 mutations cause the rare autosomal recessive diseases spinal muscular atrophy with respiratory distress type 1 (SMARD1) and Charcot-Marie-Tooth disease type 2S (CMT2S), which are characterized by severe neurodegeneration and myopathies (Grohmann et al. 2001; Cottenie et al. 2014). The disease-associated nonsense, frameshift, or missense mutations in IGHMBP2 are predicted to impair DNA/RNA binding, unwinding, and ATP hydrolysis, and thus pathogenicity is attributed to loss-of-function of IGHMBP2 enzymatic activity (Guenther et al. 2009a; Lim et al. 2012; Saladini et al. 2020). While the mechanism of cellular pathogenesis upon functional loss of IGHMBP2 is unknown, IGHMBP2-dependent translational disruption is a favorable hypothesis considering the relevance of translational dysregulation among inherited disease mechanisms (Scheper et al. 2007). For example, a prevalent cause of amyotrophic lateral sclerosis (ALS) are expansions in *C9orf72*, which lead to global translational repression that inhibits the mRNA decay activity of UPF1, another SF1 helicase (Sun et al. 2020). Defective helicases cause numerous translation-linked pathologies beyond neurodegeneration—DDX3X is a primary example of an SF2

helicase associated with neurodevelopmental disorders and cancers when its translational activities are perturbed (Bohnsack et al. 2023; Gadek et al. 2023).

To-date, the connection between IGHMBP2 and translational regulation has been evidenced by prior biochemical work and using model mice or mouse motoneurons. IGHMBP2 is predominantly cytoplasmic, where it co-localizes with translation initiation factor eIF4G2 and rRNA (Grohmann et al. 2004; Guenther et al. 2009a). Therefore, despite IGHMBP2 having *in vitro* activity on DNA or RNA, its physiological substrate may be primarily RNA. IGHMBP2 co-precipitates and co-sediments with ribosomal proteins and subunits, and thus interacts with translational machinery during translation (Guenther et al. 2009a). Localized translation, as indicated by expression of a translationally-regulated β -actin GFP-3'UTR reporter, is slowed in IGHMBP2-deficient motoneurons post-photobleaching (Surrey et al. 2018). IGHMBP2 also co-precipitates with macromolecules that contribute to translational regulation such as elongation factors and tRNA-Tyr (Guenther et al. 2009a; de Planell-Saguer et al. 2009). Mice with spontaneous IGHMBP2 mutations—which model human SMARD1 phenotypes—were found to be rescued when expressing a genetic modifier locus encoding ABT1 and several tRNA genes, further implicating a connection between tRNAs and IGHMBP2 in disease pathology (Cox et al. 1998; de Planell-Saguer et al. 2009).

Recent work has established a connection between tRNA and diverse neurodegenerative disorders. Disruption in tRNA regulatory genes via mutations in various aminoacyl-tRNA synthetases (ARS) causes several axonal types of CMT, such as CMT2N, CMT2U, CMT2W, and CMT2D, and can also cause other forms of neurodegeneration or ataxia (Lee et al. 2006). Recently, defective GARS activity in

CMT2D was found to induce ribosomal stalling and activate GCN2, triggering the integrated stress response (ISR) (Spaulding et al. 2021; Mendonsa et al. 2021). The ISR mediates cellular reprogramming toward pro-survival or apoptosis in response to various exogenous or endogenous stimuli, including translation elongation stalls due to tRNA deficiency, and is a disease mechanism among several neurodegenerative disorders (Costa-Mattioli & Walter, 2020). It is unclear whether the ISR is activated by loss of IGHMBP2.

In this study, we investigated the physiological and molecular consequences of IGHMBP2 deletion in human cells. We found that IGHMBP2 depletion causes cell proliferation and global protein synthesis to decline, supporting a role of IGHMBP2 in global translational efficiency. We defined the gene expression changes caused by loss of IGHMBP2 using RNA-seq and ribosome profiling, and found that expression of the stress-induced transcription factor ATF4 was upregulated in IGHMBP2 deletion cells. We generated ATF4 reporter cell lines to confirm the occurrence and reversibility of chronic, IGHMBP2-associated activation of the ISR. Our observation of ISR activation and translational suppression caused by IGHMBP2 deletion may point to a possible disease mechanism and solidifies a role for IGHMBP2 in translational regulation.

2.2 Results

2.2.a IGHMBP2 deletion impacts cellular proliferation and global translation

To investigate the molecular function of IGHMBP2, we deleted IGHMBP2 in K562 CRISPRi cells using CRISPR-Cas9 with two sgRNAs targeting exon 2 of *IGHMBP2* (Fig. 1A). Edited clones were screened for inactivating alleles via PCR, and selected

partial and full-knockout IGHMBP2 monoclonal cell lines were validated by Sanger sequencing and Western blot (Fig. 1B,C; Supplemental Fig. S1A-E). To determine the physiological impact of IGHMBP2 deletion, we stably expressed mEGFP in IGHMBP2 deletion clones and measured competitive proliferation relative to parental cells via flow cytometry across two weeks of cell passages. We observed decreased relative cell size and lower proliferation rates among IGHMBP2 full-deletion cells (Fig. 1D,E; Supplemental Fig. S1F,G). We confirmed mEGFP expression does not impact cell proliferation and that cell lines expressing an alternate fluorophore expressed in subsequent experiments, TagBFP, exhibited comparable proliferation results (Supplemental Fig. S1H). Expression of each fluorescent protein remained robust across the experimental timeframes (Supplemental Fig. S1I). We conclude that IGHMBP2 loss induces a modest proliferation defect in K562 cells.

The effect of IGHMBP2 on proliferation could be related to its described role in protein synthesis. We therefore assessed the impact of IGHMBP2 deletion on global translation by performing polysome profiling (Fig. 2A). Western blot of polysome fractions shows IGHMBP2 co-sediments with 40S, 60S, and 80S ribosomal species (Fig. 2B). When we quantified the area under the curve (AUC) per polysome and compared relative peak ratios per cell line, we observed mild yet reproducible enrichment of free ribosomal subunits relative to monosomes and polysomes in IGHMBP2 deletion clones, while subunit-specific abundances held constant. This suggests translational suppression caused by IGHMBP2 deletion is not due to gross ribosomal biogenesis defects (Fig. 2C). To monitor global translation rates in cell lines differentially expressing IGHMBP2 at single-cell resolution, we measured relative rates

of nascent polypeptide synthesis via an O-propargyl-puromycin (OPP) assay. We found translation was suppressed in IGHMBP2 deletion clones (Fig. 2D; Supplemental Fig. S2), consistent with the polysome profiling results. We reproduced these results in cell lines expressing transgenic mEGFP, which were initially sorted to include all GFP+ cells, and detected decreased mEGFP expression per cell in IGHMBP2-disrupted clones as an additional orthogonal measure of translational activity (Fig. 2 E,F).

2.2.b Ribosome profiling reveals differentially expressed genes in IGHMBP2 deletion cells

Modest global changes in translation can result from changes to the translation of a subset of mRNAs (Calviello & Venkataramanan et al. 2021). To determine the gene expression changes in IGHMBP2 deletion cells, we performed ribosome profiling alongside RNA-seq. Ribo-seq and RNA-seq read counts showed high correlation between replicates (Supplemental Fig. S3). We confirmed Ribo-seq data exhibited 3-nt periodicity, and the majority of reads were forward-sense stranded and mapped to coding exons as expected (Supplemental Figs. S4-S6). When broadly comparing changes between datasets, we observed an increased magnitude and number of gene expression changes in full versus partial IGHMBP2 deletion cells (Fig. 3A; Supplemental Table 1). To interpret the mode of gene regulation as a consequence of IGHMBP2 deletion, we classified genes according to adjusted p-values derived from differential expression (DE) analysis. For RNA-seq and Ribo-seq results, log₂ fold-changes (L2FC) were determined per gene relative to parental expression levels, and genes with IGHMBP2-dependent RNA:Ribo-seq interaction term changes were

classified under Δ translational efficiency (Δ TE). To gain further insight into the expression changes underlying Δ TE, Δ TE genes were categorized as translation exclusive, where only ribosome occupancy level was changed significantly per gene, or translation buffered, where only differential abundance of mRNA was observed (Chothani et al. 2019; Supplemental Table 1).

We functionally characterized genes differentially expressed among IGHMBP2 deletion clones via gene set enrichment analysis (GSEA) using fold-change data from RNA-seq and Ribo-seq DE results (Supplemental Table 2). We observed gene expression attenuation between Δ mRNA and Δ TE gene sets: translation machinery and mitochondrial gene sets were transcriptionally upregulated in IGHMBP2 deletion cells, yet suppressed in Δ TE (Fig. 3B). Developmental and homeostatic gene sets were transcriptionally suppressed, yet increased in Δ TE in IGHMBP2 deletion cells (Fig. 3C). We note that 167 out of 500 possible genes in the peptide biosynthetic process, which largely overlaps with translation gene sets, were suppressed in IGHMBP2 KO clones, comprising ribosomal machinery, translation initiation, and translation elongation factors. The regulation of developmental processes gene set was highly upregulated in TE due to IGHMBP2 deletion, comprising 306 of 854 possible genes, which broadly overlapped with upregulated genes in the anatomical structure morphogenesis gene set. Beyond sets comprising diverse signaling genes, the negative regulation of DNA-binding transcription factor gene set was also significantly upregulated with a normalized enrichment score (NES) of 1.6, reflecting 236 of 582 possible genes (Supplemental Table 2). Upon performing GSEA with ribosomal footprint fold-changes, we observed translational suppression of various homeostatic gene sets appropriately corresponding

with the hemopoietic cell type of K562 cells (Fig. 3D). Together, these data identify the genetic changes underlying morphological and translation defects observed as a consequence of IGHMBP2 deletion, again implicating translation as a process impacted by loss of IGHMBP2 (Fig. 3E).

2.2.c ATF4 is upregulated in IGHMBP2 deletion cells

Considering the recessive nature of IGHMBP2 pathology, we sought to determine the genetic changes specific to full loss of IGHMBP2 to identify possible disease-relevant targets. Of several Δ TE genes identified from our RNA:Ribo-seq analysis (Supplemental Fig. S7A), ATF4 expression was notably upregulated in genes filtered for dependence on full loss of IGHMBP2 (Fig. 4A). Upon assessing TE classification, ATF4 was classified as translation exclusive Δ TE gene only in the full IGHMBP2 KO genotype condition (Supplemental Fig. S7B-C). Induction of ATF4 is caused by translational control through two upstream open reading frames (uORF; Lu et al. 2004; Vattam & Wek 2004). We observed an enrichment of normalized reads mapped to uORF1 and uORF2 of *ATF4* in IGHMBP2 deletion clones relative to parental cells, especially at the enhancer uORF1 (Fig. 4B,C), suggesting translational activation of ATF4 expression.

To test the hypothesis that IGHMBP2 deletion is inducing ATF4 expression, we generated parental and Δ IGHMBP2 reporter cell lines stably expressing a CMV-driven (uORF1,2)-ATF4-mApple reporter gene (Fig. 4D). As part of the reporter system, a separate CMV-GFP transgene was introduced to enable normalization for promoter strength and translational activity (Guo et al. 2020). We used this reporter due to

challenges with robust detection of ATF4 via immunoblot. We detected elevated ATF4 reporter levels in IGHMBP2 deletion clones relative to parental (Fig. 4E; Supplemental Fig. S8A,B). We confirmed inducibility of reporter expression upon acute ISR stimulation via thapsigargin (Supplemental Fig. S8C). We then exogenously expressed IGHMBP2 N- or C-terminally fused with TagBFP in our IGHMBP2 deletion reporter cell lines and observed ATF4 reporter expression reversed toward parental levels of ATF4 with both transgenes (Fig. 4F; Supplemental Fig. S8D,E), indicating genetic rescue and supporting the causative nature of *IGHMBP2* genetic lesions. We therefore find that loss of IGHMBP2 induces ATF4 expression.

2.2.d IGHMBP2 deletion results in ISR activation

ATF4 is a stress-responsive transcriptional regulator that is tightly regulated at the translational level (Harding et al. 2000; Vattem & Wek 2000). Given the role of ATF4 as part of the ISR and the relevance of the ISR in neurodegenerative diseases, we wondered if activation of the ISR is a consequence of IGHMBP2 deletion. Surprisingly, differences in p-eIF2 α were not discernible between parental and IGHMBP2 deletion cells via Western blot (Supplemental Fig. S9A-B). This may be due to homeostatic regulation, which produces reduced levels of p-eIF2 α upon chronic ISR activation relative to acute stress (Novoa et al. 2003; Guan et al. 2017). However, upon treating IGHMBP2 deletion cell lines with p-eIF2 α -dependent ISR inhibitor ISRIB, ATF4 reporter expression in IGHMBP2 KO cells robustly reversed toward parental reporter levels at steady-state, supporting the occurrence of chronic, p-eIF2 α -induced ISR activation (Fig. 5A).

Four kinases can activate the ISR: PKR senses specific types of dsRNA, HRI senses mitochondrial dysfunction, PERK responds to the unfolded protein response in the endoplasmic reticulum, and GCN2 activates upon ribosome collisions induced by starvation or deficiencies in tRNA metabolism (Costa-Mattioli & Walter, 2020). Given the genetic connection between IGHMBP2 and tRNA metabolism, we hypothesized ISR activation in IGHMBP2 deletion cells could be driven by empty A-site induced ribosomal stalling and downstream GCN2 activation (Fig. 5B). We thus treated ATF4 reporter cell lines with kinase inhibitor GCN2iB (Nakamura et al. 2018) and observed a modest decrease in ATF4 reporter expression in IGHMBP2 deletion cell lines (Fig. 5C). Upon determining that ISR activation is driven by GCN2 in IGHMBP2 deletion cells, we wondered if we could detect ribosome stalling among our Ribo-seq reads, as empty A-site stalled and collided ribosomes canonically activate GCN2 (Ishimura et al. 2016; Inglis et al. 2019). We first performed a metagene analysis using Ribo-seq reads to determine whether IGHMBP2 deletion alters ribosome positioning along transcripts globally, as might occur under strong stalling conditions. We observed consistent ribosomal occupancy across sequenced transcripts in knockout compared to parental cell lines (Supplemental Fig. S10A), suggesting IGHMBP2 deletion may impact translation by a more ubiquitous mechanism non-specific to a particular stage of translation, or perhaps toward specific transcripts undetectable by global analysis. Determining whether IGHMBP2-RNA recognition or unwinding activity impacts global translation and how this may be governed by particular biophysical properties or motifs among mRNAs warrants further experimentation.

As tRNA dysregulation may be a favorable hypothesis driving global translation changes, specifically tRNA-Tyr as implicated from prior literature (de Planell-Saguer et al. 2009), we performed a Northern blot to visualize total tRNA-Tyr and tRNA-Val expression among our cell lines (Supplemental Fig. S10B). We did not discern differences in abundance of these tRNAs, suggesting IGHMBP2-dependent differences in tRNA-Tyr abundance may not occur in K562 cells or may occur below detectability among biochemical assays. To further test the hypothesis that IGHMBP2 loss affects decoding of a subset of codons, we applied a recently-developed machine learning package, *choros*, to infer in-frame ribosome A-site occupancy of codons globally, but did not detect specific codon enrichment (Mok et al. 2023; Supplemental Fig. S10C-H). This lack of signal is perhaps due to the subtle effect size of IGHMBP2 loss on translation, or could occur for other unknown reasons. We conclude IGHMBP2 deletion results in chronic, low-level ISR activation mediated by GCN2 signaling (Fig. 5D), which could reflect low-level ribosome collisions below our detection threshold.

2.3 Discussion

In this work, we defined the impact of IGHMBP2 in translation using Cas9-mediated IGHMBP2 knockout human cell lines. We also studied the effects of complete loss of IGHMBP2 expression compared to heterozygous IGHMBP2 cell lines to reflect a biologically-relevant, non-pathological regime. We show that relative to partial deletion or transgenic knock-in, full loss of IGHMBP2 slows cell proliferation, reduces translation, disrupts gene expression across the transcriptome and translome, and activates the ISR.

To further characterize ISR activation in IGHMBP2 deletion cells, we performed GSEA with a custom gene set comprising 122 compiled ATF4 target genes (Neill & Masson, 2023). While we observed enrichment in Δ TE among ATF4 target genes to a similar magnitude of top gene sets from the Biological Processes gene ontology, this result did not reach statistical significance (Supplemental Fig. S11A,B). ISR-induced apoptotic signaling typically involves CHOP upregulation (Gachon et al. 2001), which we did not detect in our DEG dataset, suggesting cellular stress caused by IGHMBP2 deletion induces a pro-survival ISR program. We notably observed chronic, low-level activation of ATF4 among our IGHMBP2 deletion cell lines, which is also associated with pro-survival ISR programming (Pakos-Zebrucka et al. 2016). We surmise IGHMBP2 deletion-induced, pro-survival ISR may enable cells to respond to upstream molecular consequences of IGHMBP2 disruption, ultimately resulting in subtle rather than severe fitness defects.

Although IGHMBP2 is ubiquitously expressed, IGHMBP2-associated pathogenesis is thought to be tissue-specific. IGHMBP2 is most highly expressed in the brain, and pathological symptoms of SMARD1 and CMT2S are restricted to neural and muscle tissue (Cox et al. 1998; Guenther et al. 2009b; Cottenie et al. 2014). We speculate this may explain the small effect sizes observed in our model in contrast to more measurable ISR effects observed in neuronal cells modeling CMT2D (Spaulding et al. 2021; Zuko et al. 2021). Alternatively, the ISR may be more strongly activated by IGHMBP2 loss in highly proliferative cells such as K562s, thus measuring ISR activation in animal models will be important work for the future. Despite the small effect sizes, we robustly and reproducibly observe modest translation repression and chronic ISR

activation using high-throughput and sensitive approaches such as deep sequencing and flow cytometry. Our work may also inform future experimental considerations toward detecting disease-relevant, chronic stress markers that may otherwise remain undetected using traditional techniques.

While tRNA metabolism-driven ISR activation is an intriguing disease mechanism hypothesis, axonal CMT is notably caused by various other sources of molecular dysfunction as well. For example, disruption in mitochondrial activity (CMT2A, CMT2DD, CMT2EE), cytoskeletal proteins (CMT2B1, CMT2E, CMT2CC), and other diverse cellular functionalities converge among CMT pathogenesis. Thus, it is feasible that alternative consequences of IGHMBP2 deletion beyond tRNA dysregulation may more dominantly contribute to neuropathy and myopathy, though it is appealing to speculate this may be tissue-dependent considering SMARD1 model mice are rescued when expressing a modifier locus encoding ABT1 and five tRNA-Tyr genes (de Planell-Saguer et al. 2009). How mechanisms of IGHMBP2-associated pathogenesis may compound or differentially manifest across different tissue types will be important to deconvolve in future studies.

Consequences of IGHMBP2-DNA impairment remain unaddressed in our study and would be important to distinguish considering IGHMBP2 is also found in the nucleus (Grohmann et al. 2004). The namesake of IGHMBP2 refers to its recognition of DNA motifs that aid immunoglobulin heavy chain recombination, and IGHMBP2 exhibits slower, short-lived dsDNA unwinding processivity *in vitro* relative to the prototypical SF1 helicase, UPF1 (Mizuta et al. 1993; Kanaan et al. 2018). Expanded functional insight toward IGHMBP2-DNA and its unique processive behavior is yet to be determined.

Whether differential transcription caused by IGHMBP2 deletion precedes cellular stress activation and translational dysregulation remains unclear, and this is confounded by transcriptional reprogramming chronically mediated by the ISR. Future DNA-binding experiments may elucidate the possible relevance of IGHMBP2-DNA disruption toward cellular pathology.

One of 95 broadly elusive, non-redundant human helicases, IGHMBP2 is an understudied non-essential gene with recent findings that shed light on its fundamental importance (Umate et al. 2011). IGHMBP2 was predicted to contribute to cellular fitness in a CRISPR screen in HEK293T cells (Hart et al. 2015), and we establish that perturbing IGHMBP2 indeed also reduces cellular fitness in K562 cells via translation suppression and ISR activation. Beyond the physiological consequences we have identified, a recent screen performed in HeLa cells showed IGHMBP2 disruption alters nucleolar dynamics, further demonstrating its ubiquitous impact across non-neuronal cellular models (Sheu-Gruttadauria et al. 2023). This study also predicted gene functionality based on how genetic perturbations influenced nucleolar dynamics, which categorized IGHMBP2 in a non-ribosomal biogenesis role that disrupts nucleolar rRNA composition, in-line as a potential consequence of IGHMBP2-associated global translation suppression. Promisingly, adeno-associated virus (AAV) therapeutic strategies have been shown to rescue SMA-related phenotypes, including SMARD1 in mice using AAV9-IGHMBP2 (Pattali et al. 2019; Shababi et al. 2016). Thus, our demonstration of reversible IGHMBP2-dependent pathologies may present a therapeutically-relevant, cell-based system for further study. Defining the fundamental function of IGHMBP2 and repercussions immediately downstream of IGHMBP2 deletion

will also be imperative for identifying alternative, drug-based therapeutics. Our work demonstrates the utility of studying neuropathy-associated gene IGHMBP2 in an immature human cell line, expands on the fundamental relevance of IGHMBP2, and reinforces the significance of translation in cellular health.

2.4 Materials & Methods

Cell culture

K562 CRISPRi cell lines used in this study were maintained in RPMI 1640 (Gibco) containing L-glutamine and 25 mM HEPES, supplemented with 10% FBS and 1% penicillin-streptomycin. Cells were stored in humidified incubators at 37 °C with 5% CO₂ and routinely checked for mycoplasma (Lonza).

Cell line generation

Cas9-mediated knockout of IGHMBP2 was performed using two sgRNAs (Synthego) to target exon 2 of IGHMBP2 in combination: 5'-CAGAGAGAUGUUCUC CUGCC-3' and 5'-CUGAAAGAGCUCCAGAGCCG-3'. Ribonucleoprotein (RNP) complexes were prepared by combining 50 pmol of recombinant Cas9 to 50 pmol of each sgRNA and incubating the mixture for 20 min at 37 °C. K562 CRISPRi cells (Gilbert et al. 2014) were nucleofected (SF Cell Line 4D kit; Lonza) with the RNP. Nucleofected clones were isolated by limiting dilution and indel-containing clonal populations were screened by extracting gDNA using Quick Extract (Biosearch Technologies) for PCR amplification using primers targeting up and downstream the Cas9 cut-site: 5'-GGTTGT GGCATTAAGTGGCC-3' and 5'-CCCACATCAATTG

TTGGAC-3'. PCR products were separated on a 3% agarose gel at 100 V, and *IGHMBP2* gDNA disruption in select clones was further validated via Sanger sequencing with primer 5'-CTTTACGAGGGTACAAGTCACGG-3' and Western blotting.

Western blot

Cell lines were harvested during active growth (0.4E6 - 0.6E6 cells/mL) and lysed in RIPA buffer supplemented with protease inhibitor cocktail (Halt). Lysates were centrifuged at 16,000 xg for 20 min at 4 °C, and total protein concentration was quantified by Pierce BCA Assay (Thermo). SDS loading buffer was added to 50 μg total protein, and samples were boiled at 95 °C for 5 min. Samples were loaded on 4-15% pre-cast PAGE gels (Bio-Rad), run at 85 V in running buffer, and transferred to a PVDF membrane (Bio-Rad). Membranes were incubated for 1 hour in blocking buffer (1% (w/v) BSA in 0.1% TBS-T), followed by an overnight incubation at 4 °C in blocking buffer containing primary antibody. Membranes were washed for 10 min 0.1% TBS-T three times, followed by a 1 hr incubation with secondary antibody with rotation at room temperature and protected from light. Membranes were washed for 10 min 0.1% TBS-T three times and imaged using an LI-COR Odyssey DLx.

Antibodies used for Western blotting include rabbit anti-IGHMBP2 at 1:500 (*Proteintech*, 23945-1-AP), rabbit anti- β -actin conjugated to AlexaFluor680 (Abcam); rabbit anti-eIF2 α at 1:1,000; rabbit anti-eIF2 α phospho-S51 at 1:1,000. Membranes were incubated with goat anti-rabbit 800 CW secondary antibody (*LI-COR*, 926-32211) at 1:10,000.

Northern blot

Northern blotting was performed using NorthernMax kit (Invitrogen) with adaptations as described. Total RNAs were extracted from K562 parental, KO clone #1 and #2 cells with Trizol reagent (Invitrogen, 15596026). 5 μ g of total RNA per sample was mixed with 100 mM final concentration of Tris-HCl (pH 9.0) and incubated for 30 min at 37 °C to remove amino acids attached to the 3' end of tRNAs. Samples were then mixed with 2X Formaldehyde Load Dye (Invitrogen, 8550G) and heat denatured for 3 min at 70 °C. RNAs were loaded onto pre-cast 10% TBE-Urea gels (Thermo Fisher, EC68755BOX) in 1X TBE. RNAs were separated by PAGE, transferred to a positively charged nylon membrane (Invitrogen, AM10104) and cross-linked to the membrane using a UV trans-illuminator (Stratalinker 2400 UV Crosslinker) for 2 min at 1200 x 100 μ J. Membranes were pre-hybridized with pre-warmed ULTRAhyb™ ultrasensitive hybridization buffer (Invitrogen, AM8670) at 52 °C for 1 hr, followed by addition of 10 pmol of each probe. The membranes were hybridized overnight and washed two times with Low Stringency Wash buffer (Invitrogen, AM8673) with rotation at room temperature for 5 min. Membranes were probed with either tRNA-Tyr, tRNA-Val, or tRNA-Val, stripped, re-probed for tRNA-Gly as an internal control, and imaged using an LI-COR Odyssey DLx.

tRNA-Tyr and tRNA-Val probes were labeled with IRDye800RD and the tRNA-Gly probe was labeled with IRDye680RD (LI-COR), respectively. Probe sequences used include Gly-sCC (5'-TCATTGGCCRGGAATYGAACCCGGGYCTCCRCGTGGWAGGCGAGAATTCTACCACTGMACCACCMAYG/*i*AzideN/C-3'); Tyr-GTA: (5'-TCC TTCGAGCCGGASTCGAACCAGCGACCTAAGGATCTACAGTCCTCCGCTCTAC

CARCTGAGCTATCGAAG/iAzideN/G-3'); Val-mAC: (5'-TGTTTCYGCCYGGTTTCG AACCRGGGACCTTTTCGCGTGTKAGGCGAACGTGATAACCACTACACTACRGAAA/iAzideN/C-3'); Val-TAC (5'-TGGTTCCACTGGGGCTCGAACCCAGGACCTTCTGCGTGTAAGCAGACGTGATAACCACTACACTATGGAAC/iAzideN/C-3') (Dittmar et al. 2006).

Transgenic cell line generation

For virus generation, Lenti-X HEK 293T cells (Takara Bio) were transfected with lentiviral packaging plasmids and transgenic constructs. Virus was harvested and clarified through a 0.45 μm filter after 3 days. Lentiviral titering was optimized to result in <50% transduction to generate cells with MOI <1, and cells were infected via centrifugation at 150 xg for 1 hr in 8 $\mu\text{g}/\text{mL}$ polybrene (EMD Millipore). After 3 days, transduced cells were selected via FACS using a 85-100 μm diameter nozzle.

Flow cytometry

Flow cytometry was performed on BD Fortessa instruments. When the high-throughput screening (HTS) 96-well plate attachment was utilized, plate parameters were set to a flow rate of 0.5-1.0 $\mu\text{L}/\text{sec}$, 20 μL sample volume, 50 μL mixing volume, 200 $\mu\text{L}/\text{sec}$ mixing speed, 2 mixes, and 200 μL wash volume. Laser parameters were adjusted to approximately 400 V for FSC, 250 V for SSC, 260 V for Violet laser detected with 450/50 bandpass filter (for BFP), 350 V for Blue detected with 530/30 bandpass filter (for mEGFP and AlexaFlour488), 580 V for YGD detected with 586/615 bandpass filter (for mApple), 520 V for YGC detected with 610/620 bandpass filter (for

AlexaFlour594), 320 V for Red detected with 670/630 bandpass filter (for AlexaFlour647).

Nascent protein synthesis assay

The Click-iT Plus OPP Protein Synthesis Assay Kit (*ThermoFisher*, C10457) was utilized as described in a 96-well format with 0.5E6 cells harvested during active growth per reaction. Cells were co-incubated with OPP in DMSO or 125 nM cycloheximide as a negative control for 30 minutes prior to fixation with 4% PFA and permeabilization with 0.25% Triton-X 100 in PBS. Cells were resuspended in PBS with 5% (w/v) FBS and differential fluorescent signal between cell lines was observed by flow cytometry.

Cell proliferation competition assay

Cell lines were seeded in 96-well plates at 1.5E5 cells/mL. In wells where transgenic cell lines were seeded with parental cells, 50% abundance of non-parental cells was targeted. Flow cytometry data was collected one day after seeding, showing 35-50% starting populations of fluorescent cells compared to parental cells. Wells were passaged for subsequent measurements every 3 days for 16 days.

Polysome profiling

Cells were grown in separate flasks in triplicate and treated with 100 µg/mL cycloheximide for 5 min. 10E6 cells were harvested per sample and lysed with a hypotonic lysis buffer (10 mM HEPES pH 7.9, 1.5 mM MgCl₂, 10 mM KCl, 0.5 mM DTT, 1% Triton X-100, 100 µg/mL cycloheximide) and trituration with a 26 G needle. Sucrose

gradients were prepared with 10% and 50% sucrose in sucrose gradient buffer (100 mM KCl, 20 mM HEPES pH 7.6, 5 mM MgCl₂, 1 mM DTT, 100 µg/mL cycloheximide). For each cell line, 100 µL lysate was layered atop the sucrose gradient, and polysomal species were separated by ultracentrifugation at 36,000 RPM for 2 hours at 4 °C. Polysome profiles were obtained via injection through a spectrophotometer at a flow rate of 2 mL/min, and absorbance was recorded at 260 nm with sensitivity set to 0.1 on the UV/Vis detector.

Ribosome profiling

Cells were seeded in fresh media 16 hr prior to harvest. Cell count was measured near 0.3E6 cells/mL per cell line at time of harvest, reflecting active growth conditions. Ribosomal footprint RNAs were obtained as previously described (Calviello & Venkataramanan et al. 2021). Cell lysates was treated with RNase I and subjected to size exclusion chromatography using MicroSpin Columns S-400 HR (Illustra). Ribosome-protected RNA was then extracted with Trizol, and RNA corresponding to the size of monosomal footprints (26-34 nt) were isolated by size selection via running RNA samples in a 15% polyacrylamide TBE-Urea gel. Footprint fragments were dephosphorylated and ligated to pre-adenylated oligonucleotide linker (NI-816: 5'-/5Phos/NNNNNTAGACAGATCGGAAGAGCACACGTCTGAA/3ddC/-3') with Mth RNA ligase. Unligated linker was removed with RecJ exonuclease. Reverse transcription was performed on linker-ligated RNA with Protoscript II (primer NI-802: 5'-/5Phos/NNAGATCGGAAGAGCGTCGTGTAGGGAAAGAG/iSp18/GTGACTGGAGTTCAGACG TGTGCTC-3'), and samples were treated with 1 M NaOH to hydrolyze remaining

RNAs. cDNA was size-selected with a 15% polyacrylamide TBE-Urea gel and circularized with CircLigase II. rRNA was depleted from the sample with a subtraction oligo pool, and cDNA was quantified via qPCR. cDNA libraries were amplified with Phusion polymerase (Forward primer NI-798: 5'-AATGATACGGCGACCACCGAG ATCTACTACTCTTTCCCTACACGACGCTC) using unique reverse index primers (Reverse primer: 5'- CAAGCAGAAGACGGCATAACGAGATJJJJJJGTGACT GGAGTTCAGACGTGTG-3') and size- selected with a 15% polyacrylamide TBE-Urea gel. The quality and concentration of amplified libraries was assessed with the Bioanalyzer and Qubit; 5 ng/sample were pooled and sequenced with the Illumina HiSeq 4000 (SE65 66x8x8x0) via the sequencing core of the UCSF Center for Advanced Technology.

RNA-seq

Total RNA was extracted from lysates using Direct-zol RNA Miniprep kit (Zymo) and NEBNext Ultra II Directional RNA Illumina Library Prep Kit (NEB E7760) with NEBNext rRNA Depletion Kit V2 (NEB E7400). RNA-seq samples were prepared with single index primers (NEB ME6609S). RNA integrity and and concentration of amplified libraries was assessed with the Bioanalyzer and Qubit; 5 ng/sample were pooled and sequenced with the Illumina HiSeq 4000 (SE65 66x8x8x0) via the sequencing core of the UCSF Center for Advanced Technology.

Sequencing pre-processing

FASTQ files were converted to FASTA format. Using *cutadapt*, adapter sequences were removed from RNA-seq and Ribo-seq sample reads, and reads were filtered to a minimum length of 22 nt. Reads were collapsed by UMI, which were then removed. Ribosomal RNAs, repeat RNAs and other non-coding RNAs were aligned against and removed with *repeatmasker* using bowtie2 2.4.1. Index files were generated using STAR 2.7.5a, GRCh38 primary assembly genome.fa file, and a GENCODE v25 .gtf annotation file with --sjdbOverhang set to 64 or 29 for RNA-seq and Ribo-seq indices, respectively. Filtered reads were then mapped to corresponding indices, generating annotated .bam files for analysis.

Sequencing analysis

RNA-seq and Ribo-seq results were analyzed using *DESeq2* library in R (Love et al. 2014). Transcript biotypes from the corresponding GTF annotation (GENCODE v25) were matched to all genes, and “rRNA” and “Mt_rRNA”-classified genes remaining after pre-processing were removed. Mapped reads were pre-filtered by performing DESeq analysis on all samples to determine the minimal filterThreshold. The minimal filterThreshold was determined to be 3.7 for RNA-seq samples and 5.8 for Ribo-seq samples, and thus genes with counts below these cut-offs were removed from corresponding datasets. DESeq was run with pre-filtered genes with independentFiltering omitted, as this widened ability to statistically contextualize DE changes among genes otherwise abundantly filtered out with high independent

filterThresholds in nuanced perturbation conditions, especially among heterozygous clones. Dispersion results were then shrunken using the *apeglm* method.

Because we compare more than two groups (parental, KO, and HET genotypes) a likelihood ratio test (LRT) was employed rather than default Wald testing, which uses standard error. The initial design used was $\sim \text{SeqType} + \text{Condition} + \text{SeqType}:\text{Condition}$, and DESeq was run using likelihood ratio testing (LRT) with a reduced design $\sim \text{SeqType} + \text{Condition}$ to derive DE results reflecting $\text{SeqType}:\text{Condition}$ (Ribo:RNA with respect to genotype). DESeq was run with filterThreshold pre-filtered genes with independentFiltering omitted. Due to the modeling design, resultant p-values are the same between KO or HET clones, and L2FC were independently determined among samples. Results were then filtered by baseMean cut-offs of >60 for RNA-seq and baseMean >40 for Ribo-seq. Genes were classified as significant for RNA-seq p-adjusted values <0.01 and Ribo-seq p-adjusted values <0.05. To further account for possible clonal artifacts and outliers, final significant DE genes among RNA-seq and Ribo-seq results must be significant in at least 2 out of 4 unique clones; genes found significant in only 1 out of the 4 clonal cell lines were filtered from the final datasets.

R packages used to assess quality control of sequencing data include *MultiQC*, *RiboprofilingQC*, and *RiboseQC*. To determine localized read mapping coverage for specific genes, such as *ATF4* uORFs, bamCoverage from *deeptools* was used to convert RNA-seq and Ribo-seq pre-processed *.bam* files to *.bigwig* files, where reads were normalized to counts per million (CPM). CPM-scaled reads were then mapped to hg38 using Interactive Genomics Viewer (IGV).

Data availability

Sequencing data is available at GEO accession number GSE248890.

Gene set enrichment analysis

Using RNA-seq, Ribo:RNA-seq, and Ribo-seq DEG lists output from DESEQ analysis, the L2FC per gene was averaged between cell lines. Mean L2FC were sorted as a ranked list, and GSEA was performed using *fgsea* and *clusterprofiler* R packages using the Biological Process sub-ontology. The minimum and maximum geneset sizes were set to 25 and 1,000, respectively. GSEA was performed with 100,000 permutations, and exported genesets reflect a p-value cutoff of 0.01. The enrichment map plot was generated using the *enrichplot* library.

Metagene analysis

Metagene analysis was performed using *ribosomeProfilingQC* library in R with .bam files and the coverageDepth function. The GENCODE v25 .gtf annotation file was used to define UTR and CDS regions. Metagene profiles were then Min-Max normalized between 0 and 1 for comparability between each clone.

Codon enrichment analysis

Ribo-seq reads were mapped to the transcriptome using STAR 2.7.5a --quantMode TranscriptomeSAM. Transcriptomic .bam files were assigned posterior probability values using RSEM (rsem-calculate-expression) with --fragment-length-mean 29 and then input into the *choros* R library. For parental and KO Clone #2

samples, A-site offset rule values were determined to be 15, 14, and 16 for frame 0, 1, and 2 for reads between lengths 29-30 nt; 15, 14, and NA for frame 0, 1, and 2 for 28 nt reads; NA, 14, and NA for frame 0, 1, and 2 for 27 nt reads, respectively. A-site offset rules were less discernible in KO Clone #1, and thus was omitted from codon enrichment analysis.

2.5 Competing Interest Statement

The authors declare no competing interests.

2.6 Acknowledgements & Author Contributions

Sequencing was performed by the UCSF CAT, supported by UCSF PBBR, RRP IMIA, and NIH 1S10OD028511-01 grants. Flow cytometry and cell sorting was performed at the UCSF Parnassus Flow Cytometry CoLab. K-562 CRISPRi cells were gifted by the Jonathan Weissman lab. We thank Matthew Taliaferro and Wilfried Rossoll for crucial conversations during the formation of this project. The authors also thank the Floor lab members for support and helpful feedback, especially Jess Sheu-Gruttadauria, Yizhu Lin, and Sam Kwok for technical advice. This work was supported by the National Institutes of Health R35GM149255 (to S.N.F.). S.N.F. is a Pew Scholar in the Biomedical Sciences, supported by The Pew Charitable Trusts.

Author contributions: J.E.P generated cell lines, performed experiments, and conducted data analysis. H.D. supported initial knockout cell line characterization, Western blotting, and polysome profiling. J.L. supported sequencing pre-processing. S.G. performed Northern blotting. Z.J. and A.X. shared computational expertise and

provided technical support toward cloning and cell culture. All authors contributed thoughtful discussion. J.E.P and S.N.F co-conceptualized experiments and co-wrote the manuscript, which was revised by all authors. S.N.F. acquired funding and supervised the project.

Figures

Park_Fig1

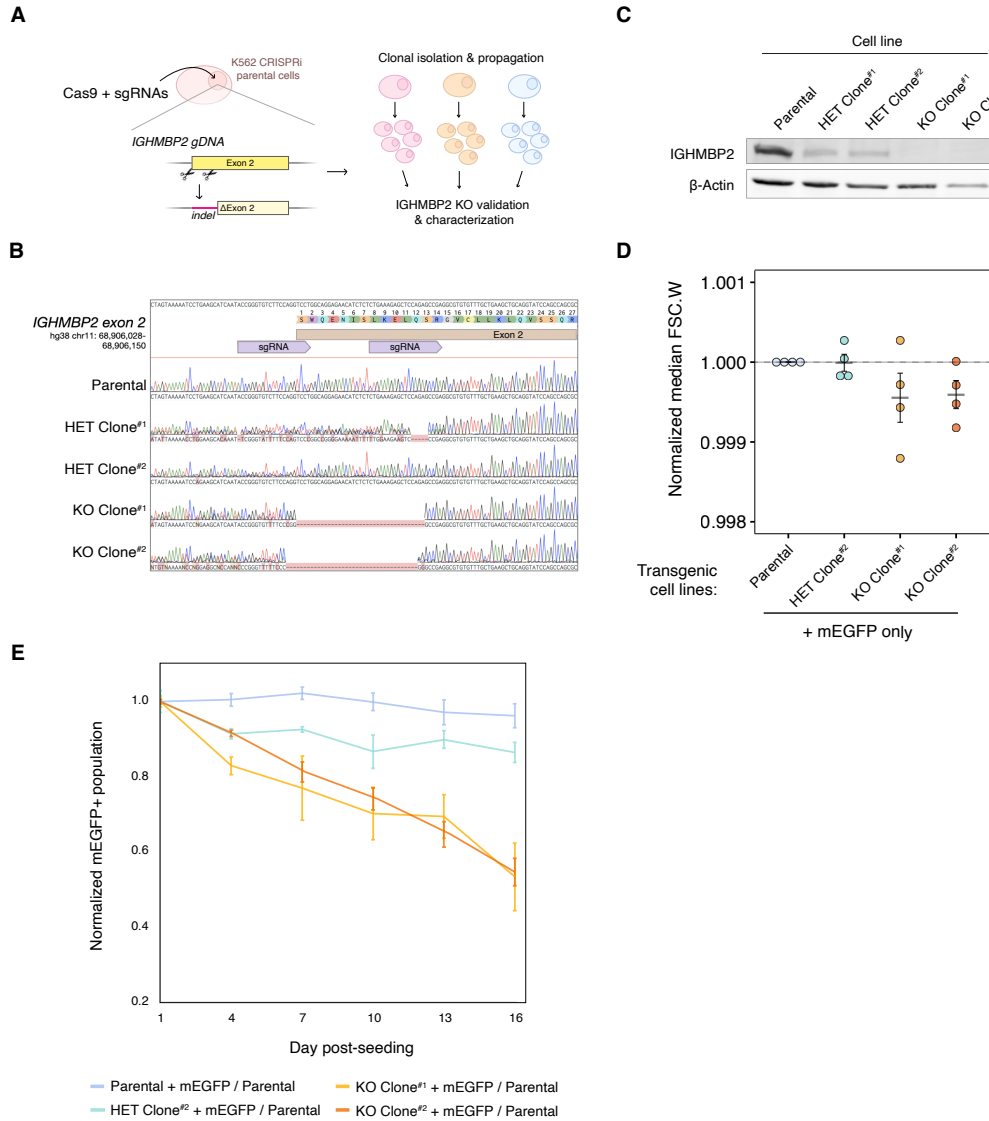


Figure 1. IGHMBP2 deletion decreases proliferation of cells.

(A) Cas9-mediated IGHMBP2 deletion in K562 CRISPRi cells. (B) Sanger sequencing of gDNA surrounding IGHMBP2 exon 2 cut-site in clones screened for indels via PCR. sgRNA guide sequences used to dually target Cas9 are indicated in purple. (C) Western blot of IGHMBP2 expression in clones depicted in B, validating reduced IGHMBP2 protein levels in HET Clones #1 and #2 and full deletion in KO Clones #1 and #2. (D) Forward-scatter width medians between cell lines with differential IGHMBP2 expression normalized to the median FSC.W of parental cells per day of measurement. (E) Competitive proliferation profiles between Δ IGHMBP2 cell lines stably expressing mEGFP seeded with 50% non-fluorescent parental cells. Each sample was seeded in triplicate on Day 0 and independently passaged on each day of measurement. Error bars reflect the coefficient of variation among of mEGFP+ populations normalized to the mean Day 1 reading among triplicate wells per sample.

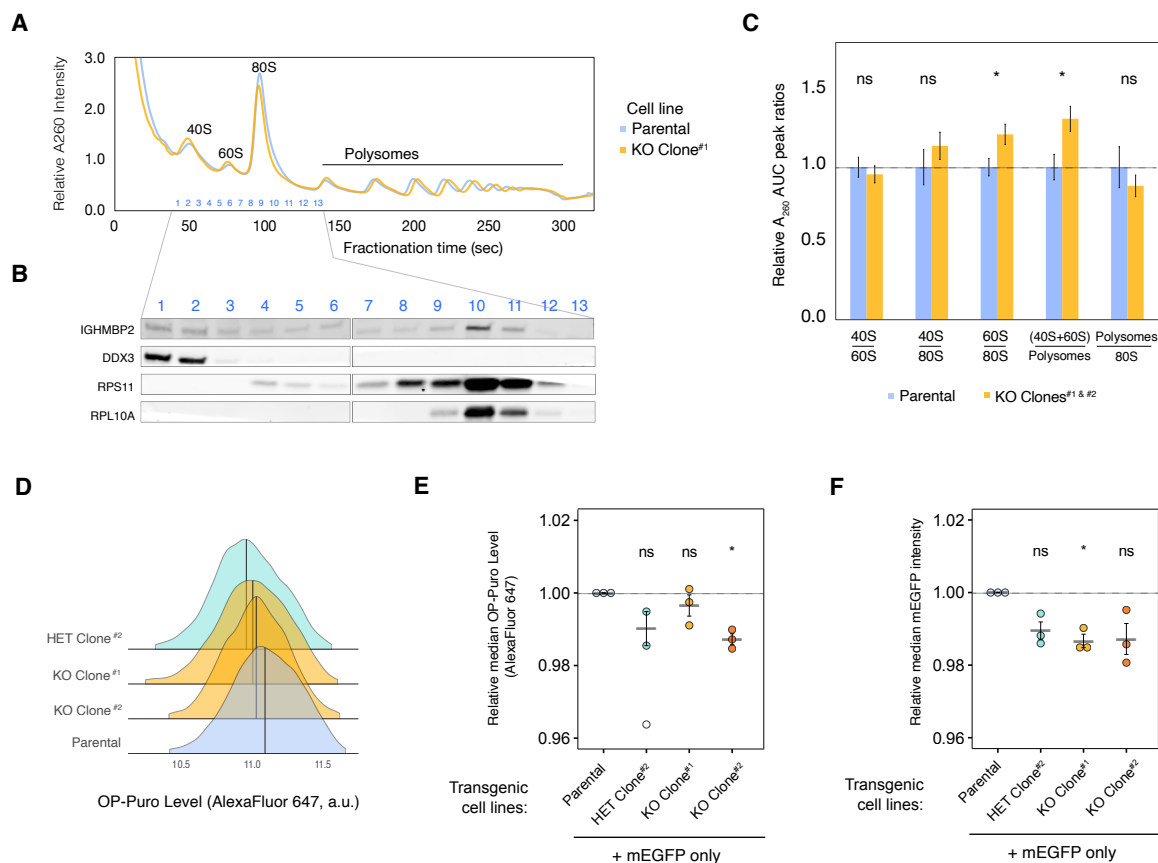


Figure 2. IGHMBP2 deletion reduces global translation in cells.

(A) Representative polysome profiles from parental K562 CRISPRi (blue) and IGHMBP2 KO Clone (yellow). (B) Western blot of fractions of the polysome profile in A. (C) Area under the curve (AUC) quantification of polysome profiles, where $n = 5$ for parental samples and $n = 7$ for IGHMBP2 deletion clone samples collected from separate flasks and measured across 3 different days. Unpaired, two-tailed, two-sample t-test between parental and KO samples per AUC ratios shown was performed to determine significance, and error bars represent standard error of the mean (SEM). (D) Representative OP-Puro (OPP) levels of cell lines used in this study quantified via flow cytometry, which was performed in 3 independent experiments with either AlexaFluor 647 as shown or AlexaFluor 594 (Fig. S2) (E) OPP assay results using cell lines expressing mEGFP only. Values beyond 2.5 standard deviations (SD) from the mean of all data points were considered outliers omitted in statistical measurement (SD = 2.6 for single outlier in HET clone; unfilled). (F) Relative mEGFP expression in samples from E. For E and F, $n = 3$, where n represents median fluorescence of single-cell intensities normalized to the median fluorescence of parental cells from experiments on 3 separate days. Horizontal black lines per each sample represent the mean, and error bars are SEM. Median values were derived from at least 10,000 cells measured by flow cytometry. Unpaired t-test was performed to determine significance. For C, E and F, ns: $p \geq 0.05$, *: $p \leq 0.05$.

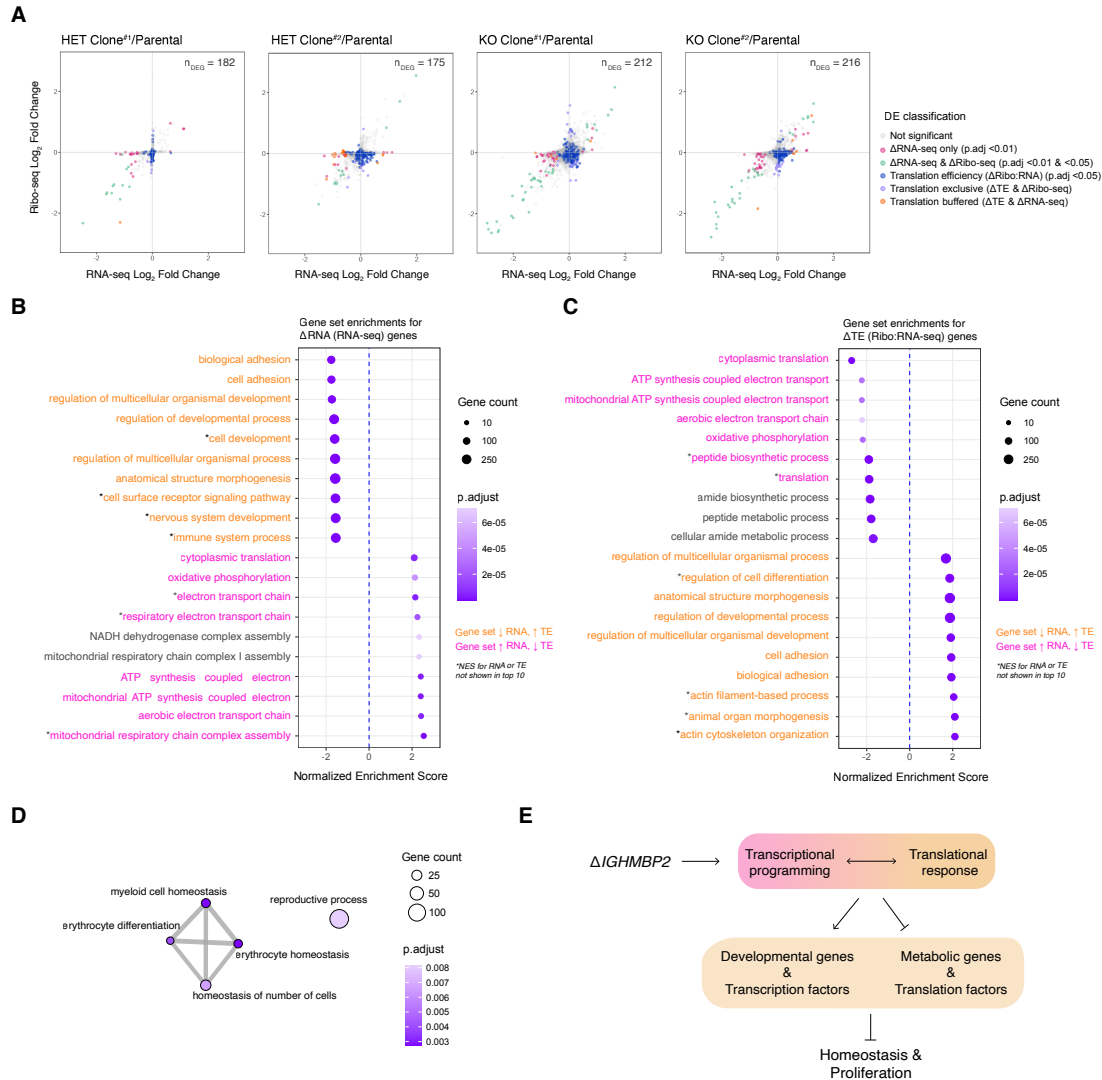


Figure 3. IGHMBP2 loss alters translation of diverse mRNAs.

(A) Ribosome profiling versus RNA-seq-derived shrunken \log_2 (Fold Change) (L2FC) per gene in clones with partial or full IGHMBP2 deletion compared to parental cells. Differential expression (DE) analysis was performed using Wald test, and p-values were adjusted (p.adj) via Benjamini-Hochberg method. Cut-offs used for DE classifications are p.adj < 0.01 for Δ RNA-seq (pink, green, and orange), and p.adj < 0.05 for Δ Ribo-seq (green & violet) and Δ translation efficiency (Δ TE; blue, violet, and orange). Genes with Δ TE across all clones were identified via likelihood ratio test against the Ribo:RNA-seq interaction term across all samples. Genes of both Δ TE and Δ Ribo-seq are identified as translation exclusive (violet). Genes of Δ TE and Δ RNA-seq are classified as translation buffered (orange). The number of DEGs (n_{DEG}) are shown per cell line. (B) Top 10 up versus down-regulated gene set enrichments (GSE) using ranked DEGs from RNA-seq and (C) Ribo:RNA-seq. GS labels are orange or pink if expression trends between B and C are opposing positively or negatively, respectively. (D) Enrichment network map of GSEA with Ribo-seq reads. In B, C, and D, GSEA was computed using the Biological Processes ontology; min GS size = 25, max GS size = 1,000 with 100,000 permutations. (E) Overview of physiological impact of IGHMBP2 disruption.

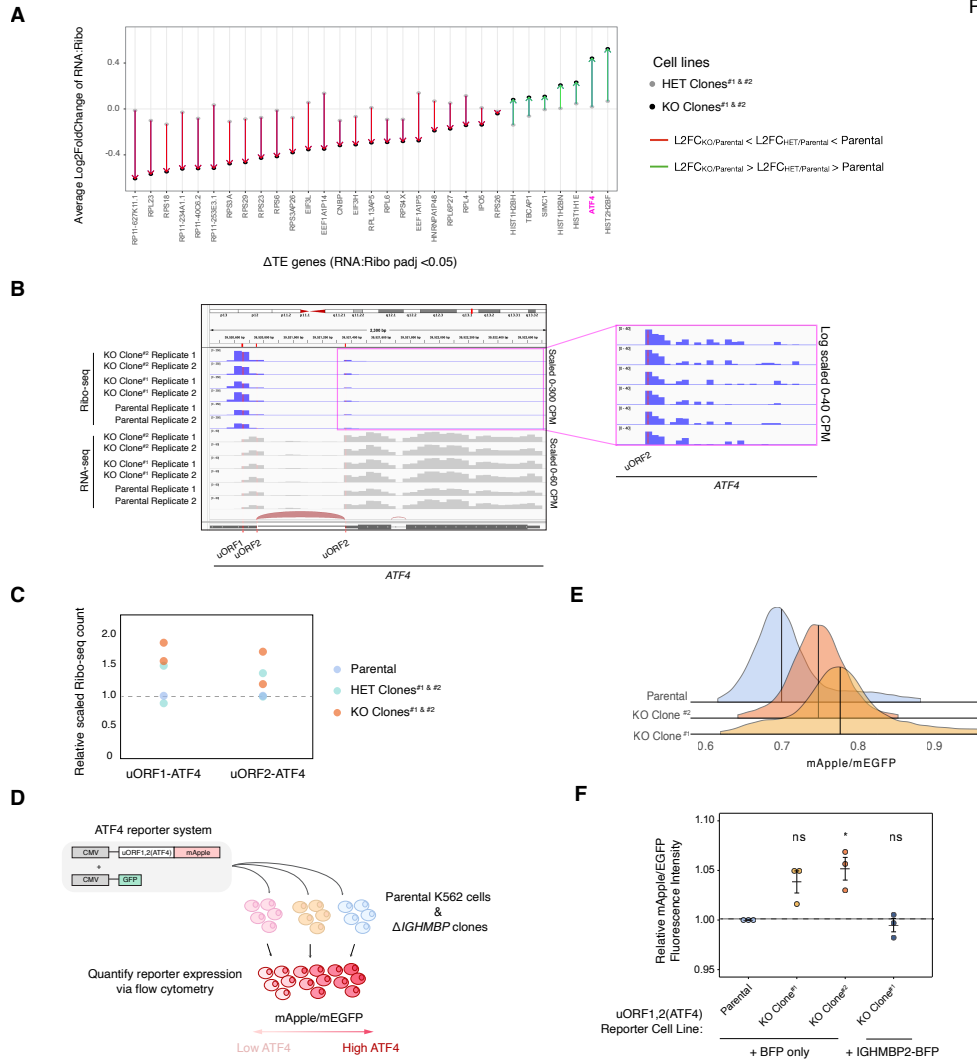


Figure 4. ATF4 is upregulated in IGHMBP2 deletion cells.

(A) Average L2FC of a subset of Δ TE DE genes in heterozygous and full deletion clones relative to parental cells. DE genes were filtered to represent those of <10% FC in heterozygous IGHMBP2 cells, where L2FC in HET clones were intermediate relative to KO results. (B) Mapped reads normalized to counts per million surrounding the 5'-UTR of *ATF4*. (C) Quantification of reads aligning to either of the two uORFs in *ATF4* in the parental, HET clones, and KO clones. Each dot represents the average scaled count per clones between two replicates. (D) Schematic of ATF4 reporter system. Transcription of lentivirally-integrated mApple and GFP reporter constructs is driven by separate CMV promoters. An ISR-sensitive, synthetic 5'-UTR encoding two uORFs (derived from *ATF4*) is upstream of the mApple ORF. (E) uORF1,2(*ATF4*)-mApple expression normalized to promoter and translational activity (mEGFP) in Δ IGHMBP2 K562 reporter cell lines. (F) Relative median mApple/mEGFP intensities among reporter cell lines expressing BFP or IGHMBP2-BFP. Single-cell mApple/mEGFP signals were normalized to the median mApple/mEGFP of parental cells from 3 different days ($n = 3$). Median values were derived from at least 10,000 cells measured by flow cytometry. Unpaired t-test was performed to determine significance (ns: $p \geq 0.05$, *: $p \leq 0.05$, **: $p \leq 0.01$).

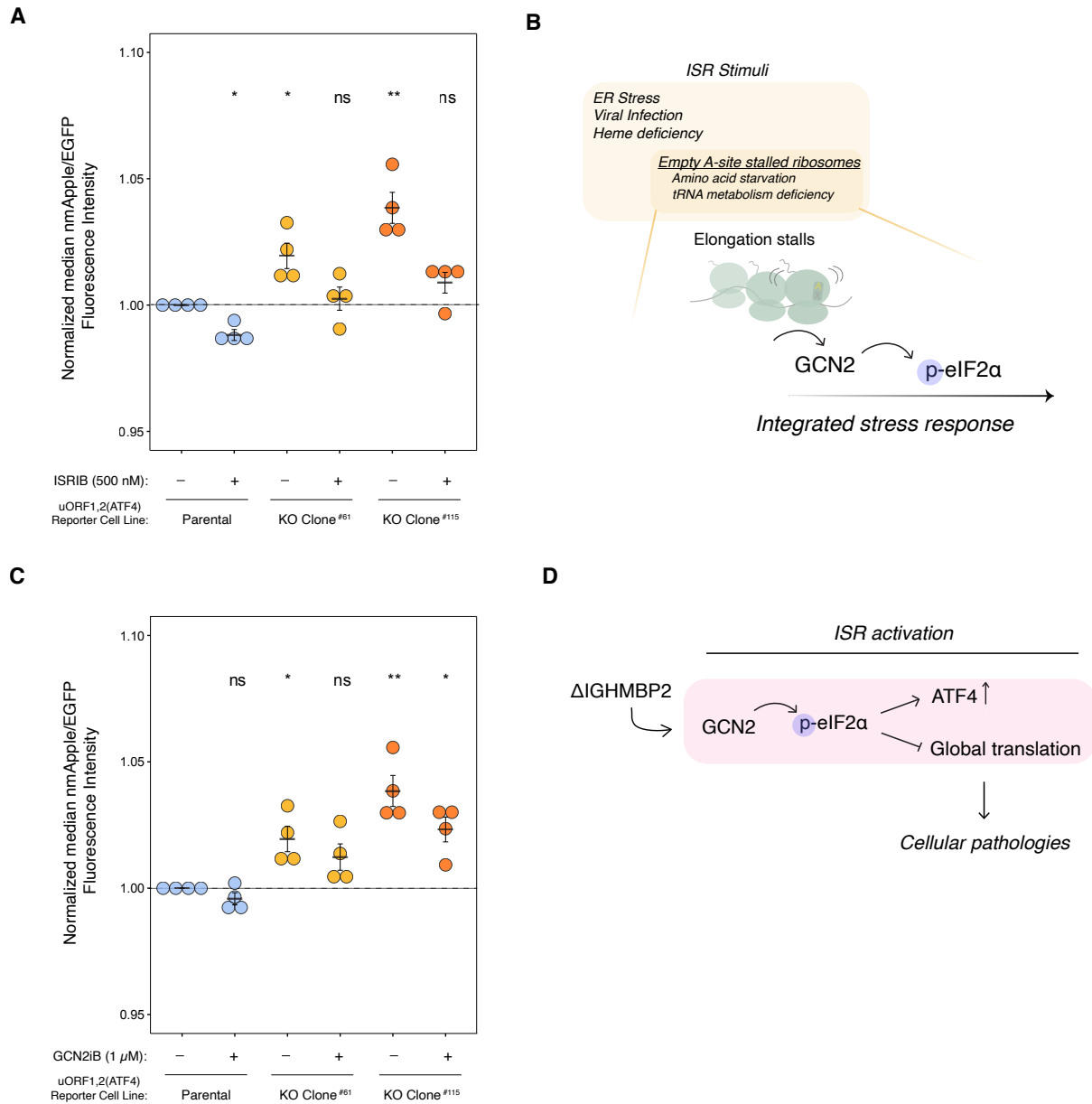


Figure 5. The ISR is activated in IGHMBP2 deletion cells.

(A) Relative median mApple/mEGFP fluorescence intensities among reporter cell lines treated with 500 nM ISRIB for 24 hr, where single-cell mApple/mEGFP signals were normalized to the median mApple/mEGFP of untreated (DMSO only) parental cells. (B) Schematic of GCN2-mediated ISR activation. (C) Relative median mApple/mEGFP fluorescence intensities among reporter cell lines treated with 1 μM GCN2iB for 24 hr, normalized as described in A. For A and D, $n=4$ where n reflects results from separate experiments performed on different days, and error bars represent SEM. Unpaired t-test was performed to determine significance (ns: $p \geq 0.05$, *: $p \leq 0.05$, **: $p \leq 0.01$). (D) A model of how IGHMBP2 deletion results in chronic ISR activation.

Supplemental Figures

To help orient the reader, the following list details how supplemental figures relate to the main figures and manuscript.

Figure 1. IGHMBP2 deletion decreases proliferation of cells.

- Figure S1. IGHMBP2 deletion clone characterization and genotyping.
 - Fig. S1. contains evidence of cell line genotyping conducted by PCR and TIDE alignment. Clone characterization is further supported with additional morphological profiles. Transgenic cell lines expressing mEGFP and alternatively BFP are utilized in subsequent experiments throughout the study, and thus similar behavior and stable free fluorescent protein expression among these cell lines is also shown in this figure.

Figure 2. IGHMBP2 deletion reduces global translation in cells.

- Figure S2. Nascent polypeptide synthesis assay with parental versus IGHMBP2 deletion clones.
 - Fig. S2. demonstrates log growth phase of cell line that OPP data reflects, while also showing additional replicate and control data for parental clone experiment (expanding on representative data shown in Fig. 2D). These experiments were also performed with the same OPP assay kit, yet using a different fluorophore (AlexaFluor594). Subsequent data in the main figure utilize transgenic cell lines performed in triplicate.

Figure 3. IGHMBP2 loss alters translation of diverse mRNAs.

- Figure S3. RNA-seq and Ribo-seq count correlation between replicates.
 - Spearman correlations between replicate sequencing count data are shown.
- Figure S4. Periodicity profiles of Ribo-seq samples.
 - 3-nt periodicity is demonstrated for all Ribo-seq samples.
- Figure S5. Strand-sense analysis among Ribo-seq samples.
 - Forward-sense mapping majority is demonstrated for all Ribo-seq samples.
- Figure S6. Read-mapping classifications of Ribo-seq samples.
 - Distribution of read-mapping among genomic features for all Ribo-seq samples is shown, where most reads for all samples map to CDS or other exon regions. Read-mapping to UTRs or other intergenic regions is also highly represented, with the lowest read-mapping categories comprising introns or other up- and down-stream genomic sequences.
- Supplemental Table 1: DEG lists
 - Differential expression data determined using DESEQ for all genes per cells lines differentially expressing IGHMBP2.
- Supplemental Table 2: GSEA lists
 - Gene set enrichment data determined using DEG data for cell lines differentially expressing IGHMBP2.

Figure 4. ATF4 is upregulated in IGHMBP2 deletion cells.

- Figure S7. Translational efficiency of ATF4 is differentially upregulated in IGHMBP2 deletion cells.
 - The expanded version of Fig. 4A is shown, which visualizes genes not filtered based on non-linear expression between parental, HET, and KO cell lines, as well as genes differentially expressed beyond 10% fold-change in HET clones. This visual may be of interest to readers who wish to see the full scope of partial and full-deletion consequences to IGHMBP2-dependent DEG. The position of ATF4 among Ribo-seq versus RNA-seq plot is also shown to further demonstrate differential translation between cell lines with HET and KO expression genotypes.
- Figure S8. ATF4 reporter cell line characterization.
 - The gating strategy for ATF4 reporter cell lines is shown. ATF4 expression corresponds with mApple, while GFP reports promoter strength and thus overall transcriptional and/or translational activity of cells. The correlation between reporters in parental cells is most linear compared to either KO clone reporters as expected from a linear relationship between transcript abundance and transgene expression, which may also reflect leaky reporter activity. In KO clones, mApple versus GFP expression is less linear, which suggests the occurrence of non-homeostatic mechanisms that may impact expression of either reporter. Positive control experiments with the promoter are shown by treatment with ER stressor & ISR-inducer thapsigargin. IGHMBP2 fused to BFP was subsequently introduced to reporter cell lines, where mApple/GFP reporter activation is shown to rescue to parental levels (expanding on Fig. 4F). The gating strategy for BFP+ cells is then shown.

Figure 5. The ISR is activated in IGHMBP2 deletion cells.

- Figure S9. Differential p-eIF2 α levels at steady-state in IGHMBP2 deletion clones is not detected by Western blot.
 - Western blots conducted using PAGE or Phos-Tag separation methods show indiscernible differential p-eIF2 α , which may suggest low-level p-eIF2 α reflective of chronic, low-level, pro-survival ISR.
- Figure S10. Ribosome footprint analyses across transcript regions and codons.
 - We demonstrate various attempts to interrogate the mechanism of GCN2-dependent ISR activation. To follow-up prior literature that implicates IGHMBP2 in metabolism of tRNA-Tyr or other tRNAs, we conducted a Northern blot using RNA extracted from IGHMBP2 KO clones versus parental cells and hybridized against tRNA-Tyr, tRNA-Val as an additional target, and tRNA-Gly as an internal control, yet did not detect discernible differences in abundance of tRNA-Tyr or tRNA-Val compared to tRNA-Gly. Using Ribo-seq data, show metagene analysis profiles for IGHMBP2 partial and full-deletion cells relative to parental, which demonstrate similar ribosomal occupancy across relative CDS regions and both UTRs. Differential A-site analysis results are also shown using Ribo-seq data, demonstrating no codon-specific occupancy could be detected from.

- Figure S11. GSEA with ATF4 target gene list.
 - To expand further upon DEGs downstream of ATF4 activation that may further inform IGHMBP2-dependent ISR mechanism, GSEA with a custom ATF4 target list was performed using Ribo:RNA-seq fold-changes. Visualization of the ranked gene list result trends suggest translational activation of select genes shown in a table, although not significant. Repeating this analysis using RNA-seq fold-changes are much less suggestive of transcriptional expression changes, suggesting ATF4-target genes may be differentially translationally regulated in IGHMBP2 deletion cells upon transcriptional activation by ATF4.

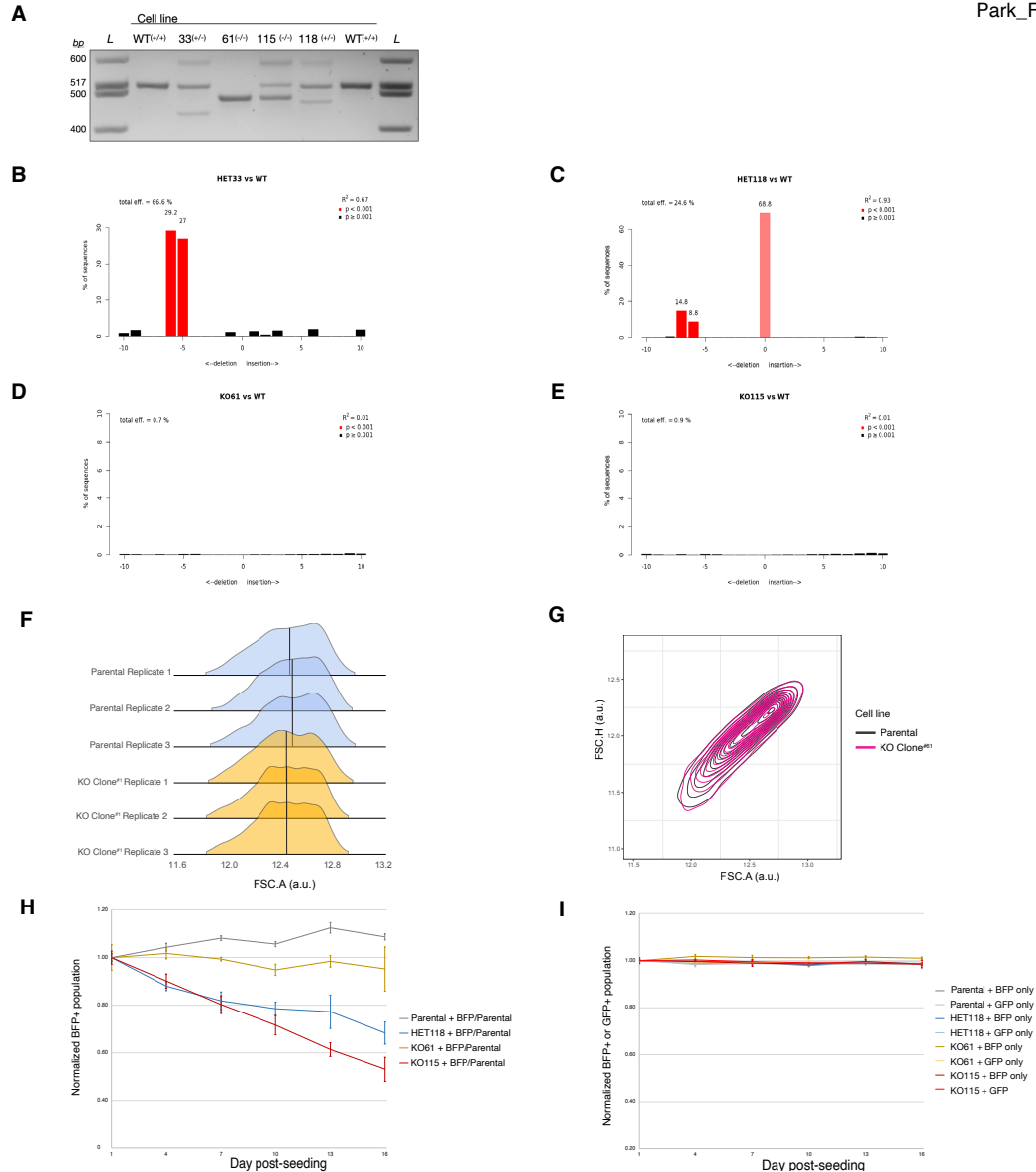


Figure S1. IGHMBP2 deletion clone genotyping and characterization.

(A) Genotyping of select clones via PCR around IGHMBP2 Exon 2 cut-site. (B-E) TIDE alignment of Sanger sequencing results quantifying indel frequencies among alleles. (F) Forward-scatter area versus height profiles between representative IGHMBP2 KO Clone#1 and parental cells. (G) Forward-scatter area versus height profiles between representative IGHMBP2 KO Clone#1 and parental cells. (H) Competitive proliferation profiles between Δ IGHMBP2 cell lines stably expressing BFP seeded with 50% non-fluorescent parental cells. Each sample was seeded in triplicate on Day 0 and independently passaged on each day of measurement. (I) Measurement of BFP+ population over 2 weeks in cell lines expressing transgenic BFP or GFP. For G and H, error bars reflect the standard deviation of BFP+ populations normalized to the mean Day 1 reading among triplicate wells per sample.

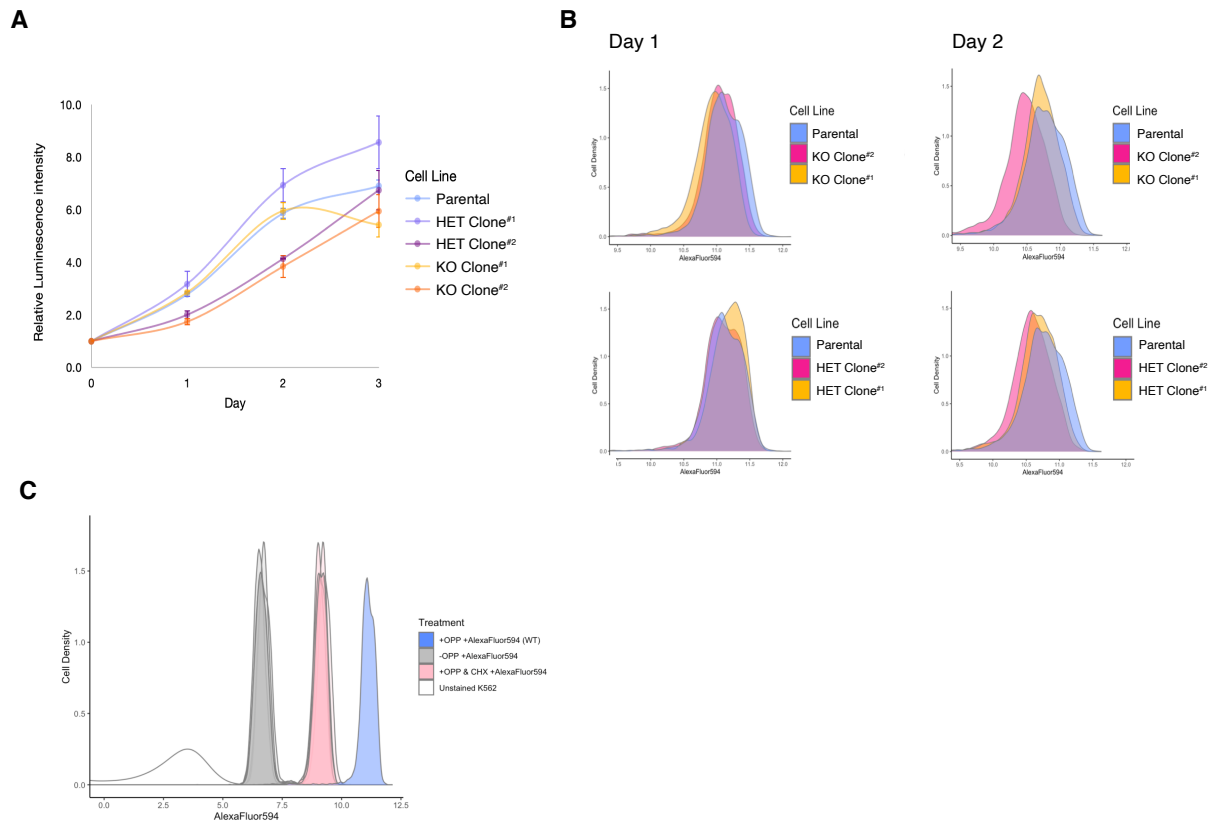


Figure S2. Nascent polypeptide synthesis assay with parental versus IGHMBP2 deletion clones.

(A) Growth rate profiles of K562 cell lines via CellTiter-Glo metabolic assay. Error bars are standard deviation between technical replicate luminescence readings. (B) Relative levels of global translation between K562 CRISPRi parental cells versus full or partial KO of IGHMBP2 as a function of AlexaFluor594 intensities via nascent protein synthesis assay, measured by flow cytometry. Cells were harvested at growth timepoints Day 1 and 2 reflected in A. (C) Representative OPP assay control results showing dynamic range between unstained, cells stained with AlexaFluor594 only without OPP, cycloheximide-treated cells, and +OPP+AlexaFluor594 cells treated with only DMSO.

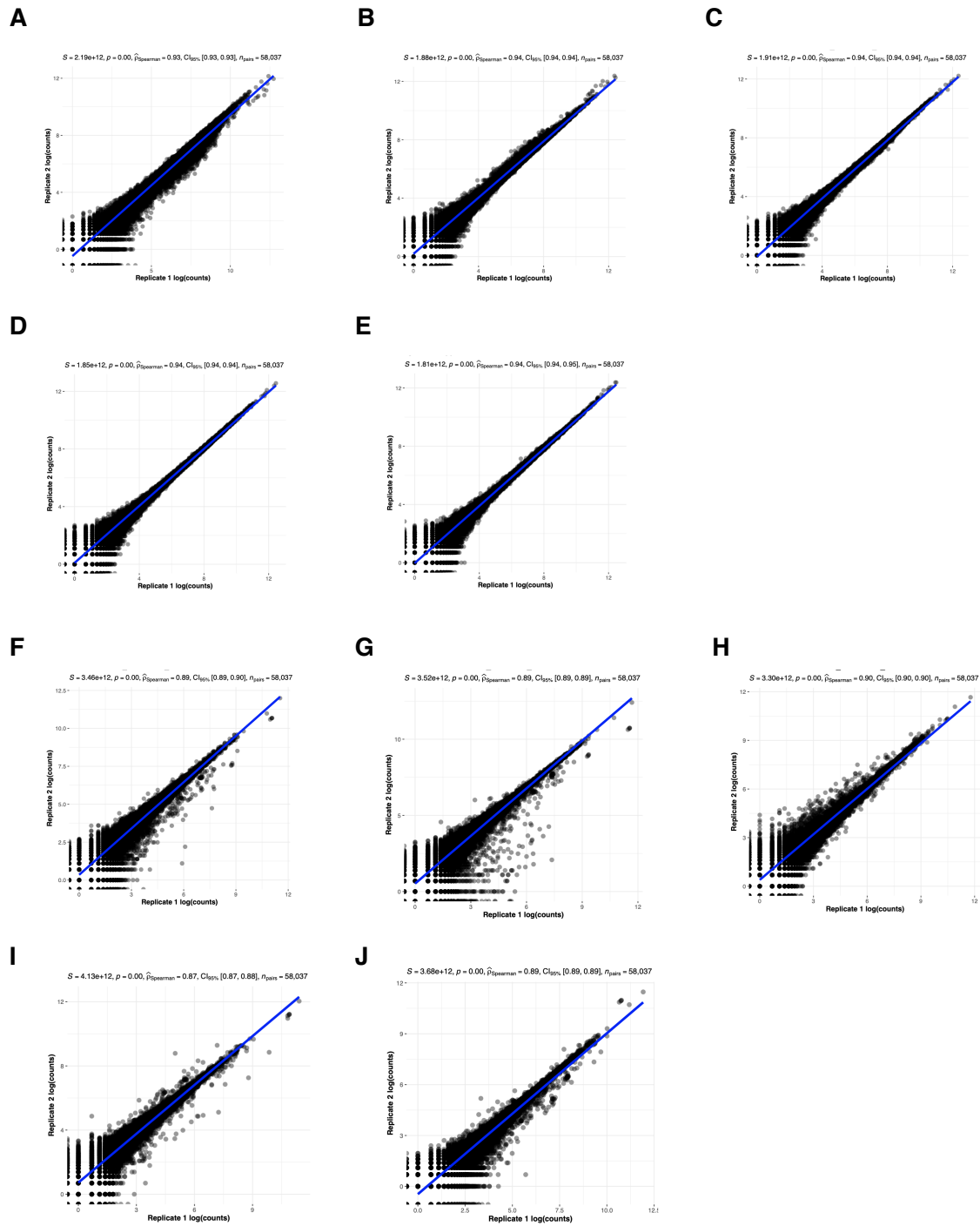


Figure S3. RNA-seq and Ribo-seq count correlation between replicate samples.

(A) RNA-seq Spearman's correlation analysis between parental, (B-C) HET Clones #1 and #2, and (D-E) KO Clones #1 and #2, respectively. (F) RNA-seq Spearman's correlation analysis between parental, (G-H) HET Clones #1 and #2, and (I-J) KO Clones #1 and #2, respectively.

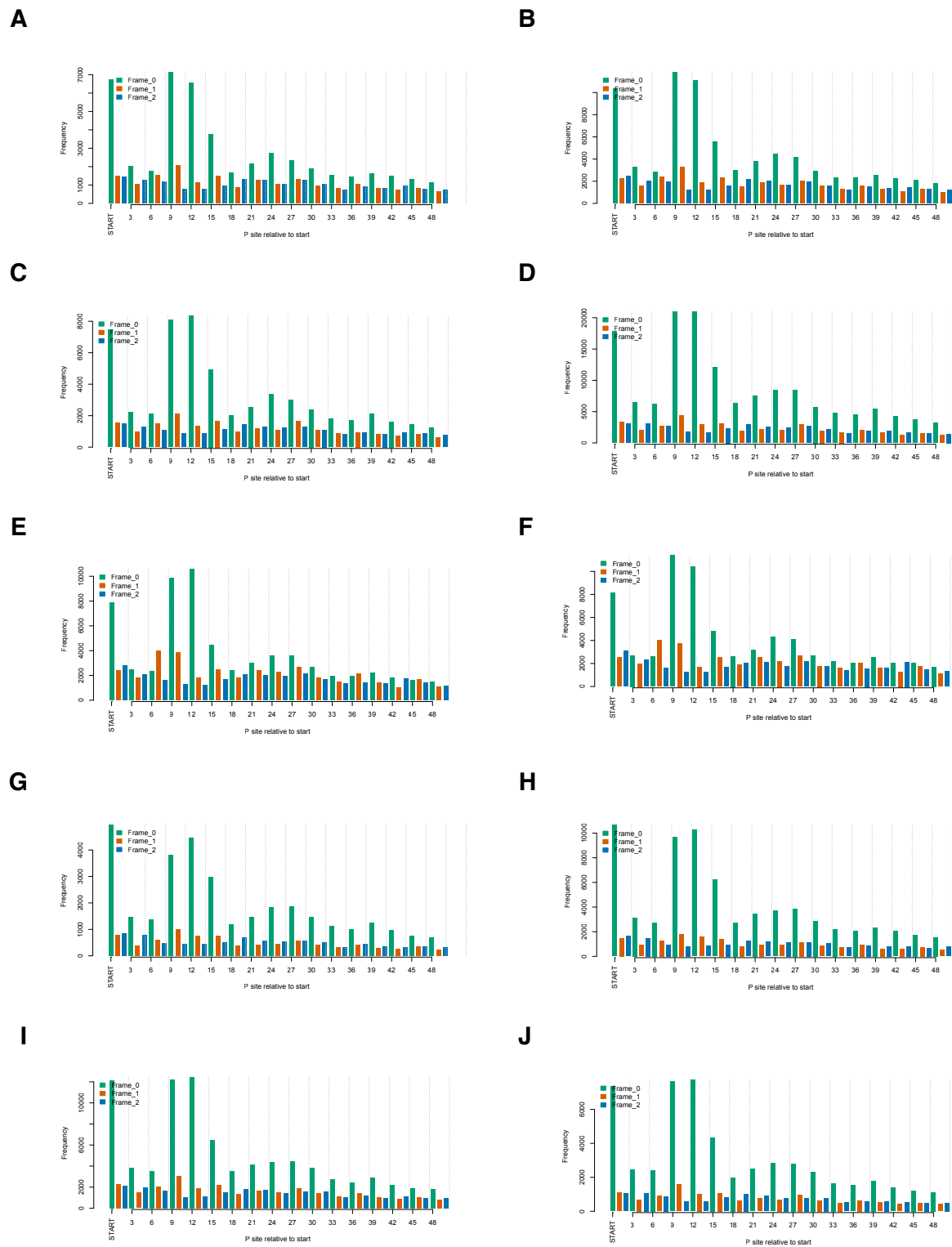


Figure S4. Periodicity profiles of Ribo-seq samples.

(A-J) 3-nt periodicity is shown for replicates 1 and 2 of Parental, HET Clone #1, HET Clone #2, KO Clone #1, and KO Clone #2, respectively.

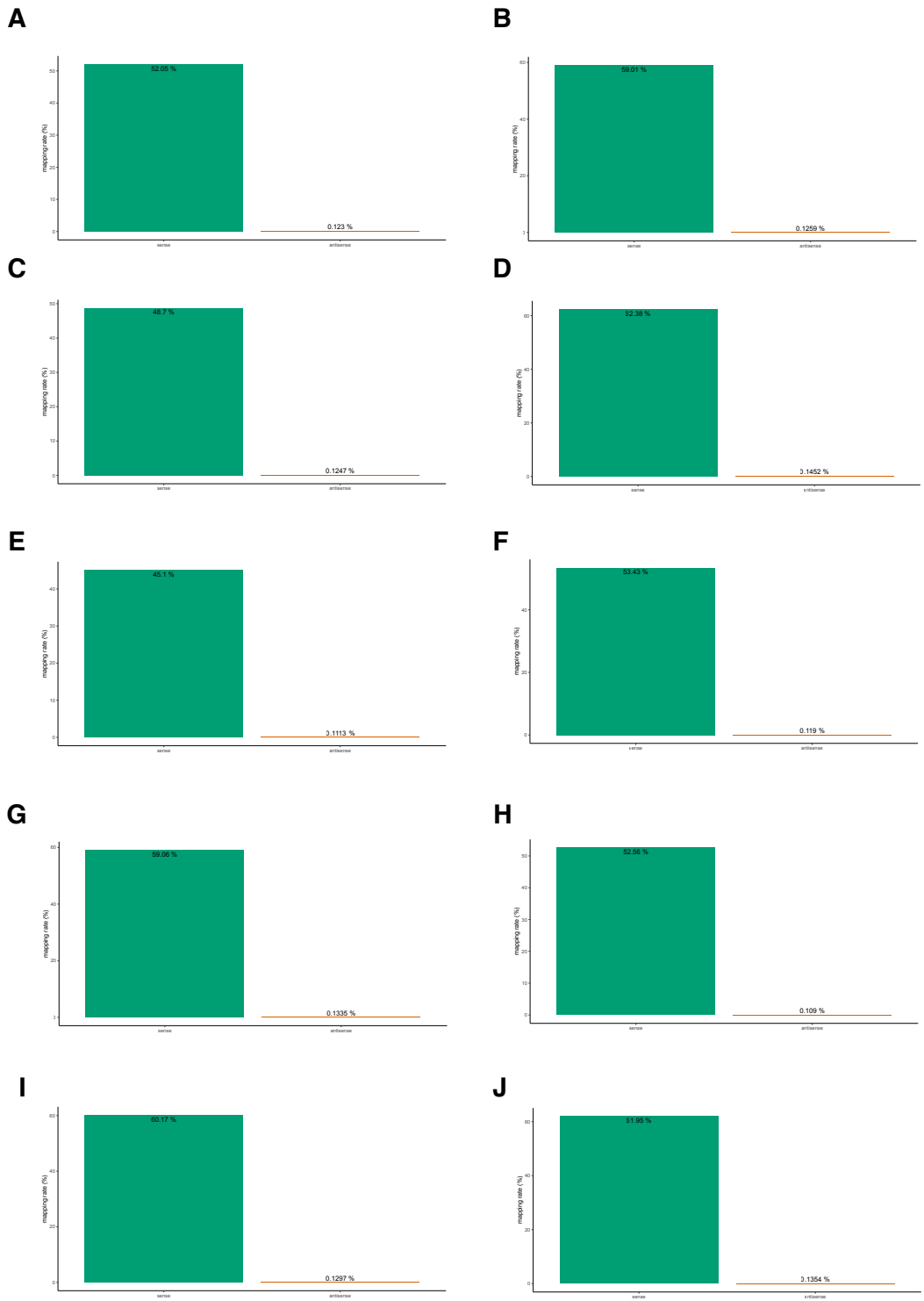


Figure S5. Strand sense analysis among Ribo-seq reads.

(A-J) Strand sense quantification is shown for replicates 1 and 2 of Parental, HET Clone #1, HET Clone #2, KO Clone #1, and KO Clone #2, respectively.

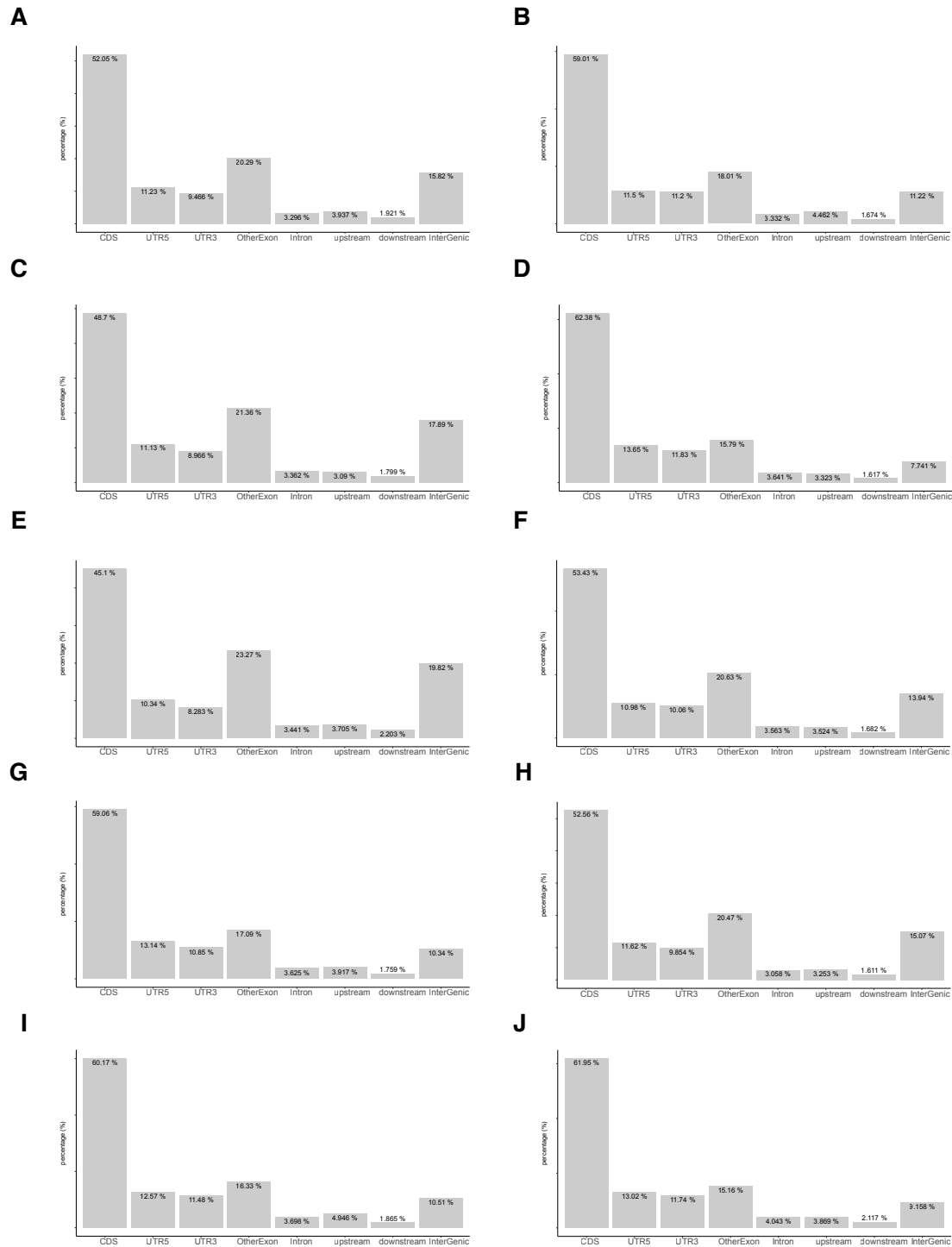


Figure S6. Read-mapping classifications of Ribo-seq samples.

(A-J) Read distributions among CDS, UTR, and other genomic classifications shown for replicates 1 and 2 of Parental, HET Clone #1, HET Clone #2, KO Clone #1, and KO Clone #2, respectively.

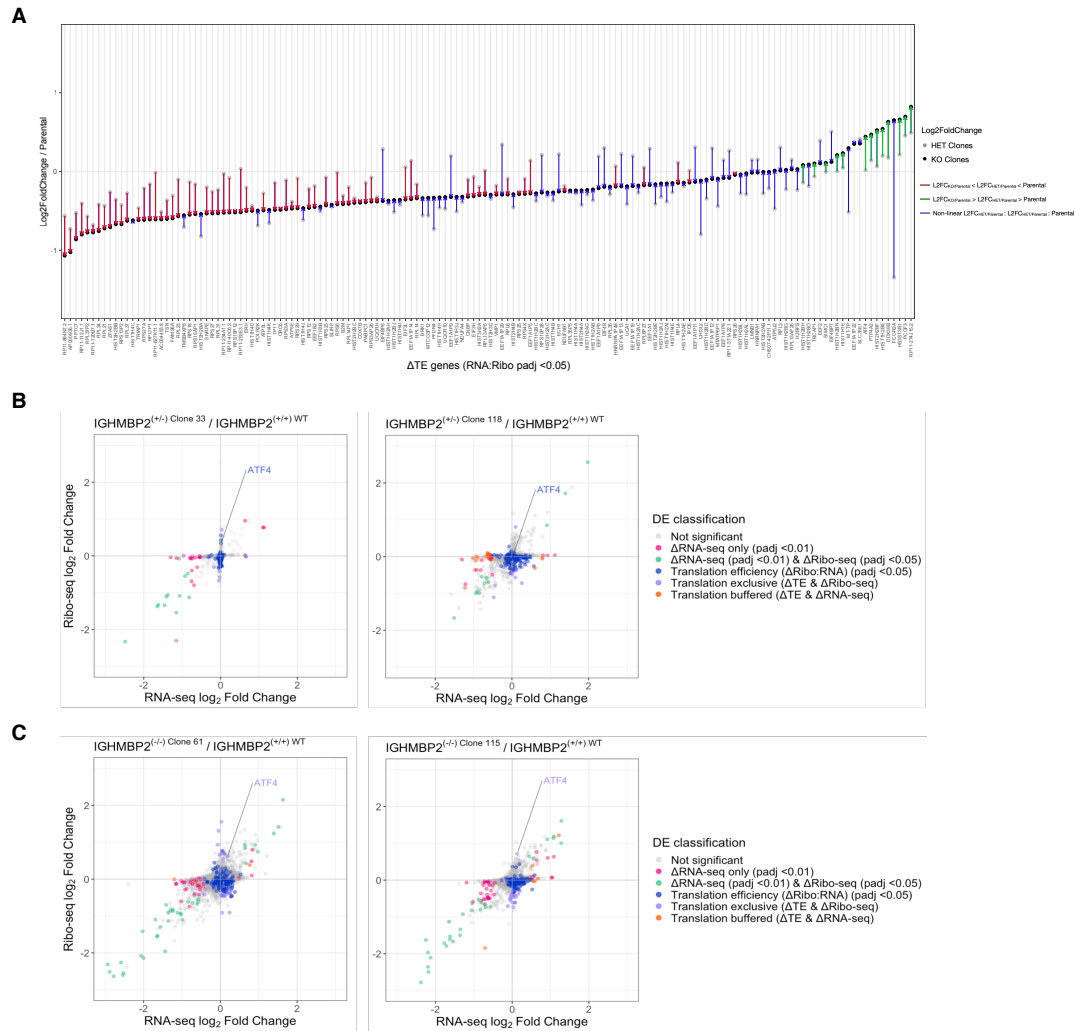


Figure S7. Translational efficiency of ATF4 is differentially upregulated in IGHMBP2 deletion cells.

(A) Average L2FC of TE DEGs in heterozygous and full deletion clones relative to parental cells. DEGs are sorted low to high average L2FC among KO clones. Average L2FC among HET clones were then plotted and connected with lines colored by relative directionality between KO, HET, and parental conditions, where linear changes are colored red or green for down and up-regulation with respect to parental, or blue for non-linear scenarios. (B) Ribosome profiling versus RNA-seq-derived shrunken L2FC per gene in clones with partial or (C) full IGHMBP2 deletion compared to parental cells. *ATF4* is highlighted, demonstrating translation-exclusive classification is gained in IGHMBP2 KO clones with reproducible Ribo:RNA-seq positioning trends. Differential expression (DE) analysis was performed using Wald test, and p-values were adjusted (p.adj) via Benjamini-Hochberg method. Cut-offs used for DE classifications are p.adj <0.01 for Δ RNA-seq (pink, green, and orange), and p.adj <0.05 for Δ Ribo-seq (green & violet) and Δ translation efficiency (TE; blue, violet, and orange). Genes with Δ TE across all clones were identified via likelihood ratio test against the Ribo:RNA-seq interaction term. Genes of both Δ TE and Δ Ribo-seq are identified as translation exclusive (violet). Genes of Δ TE and Δ RNA-seq are classified as translation buffered (orange).

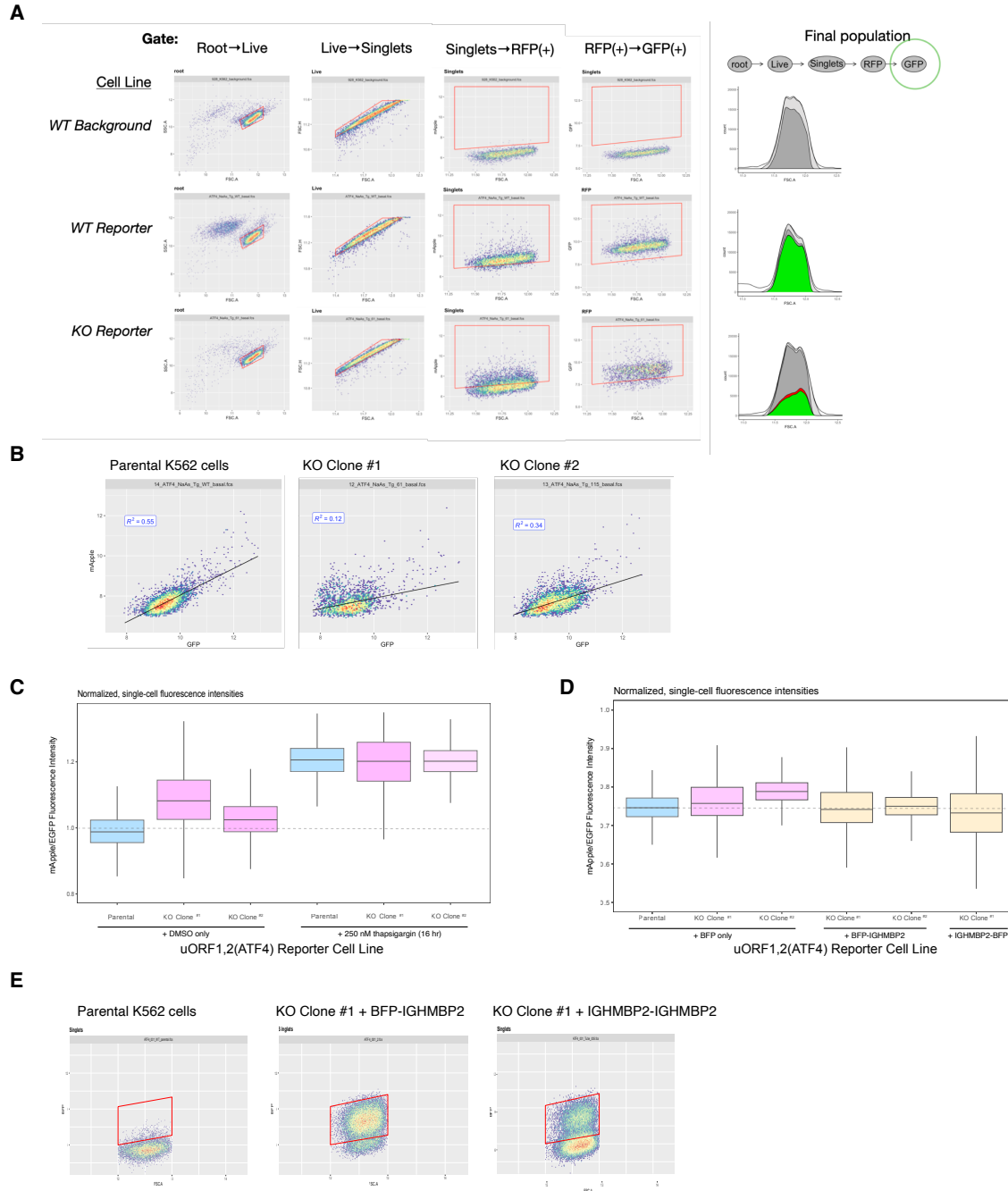


Figure S8. ATF4 reporter cell line characterization.

(A) Gating strategy for fluorescent signals of ATF4 reporter cell lines measured via flow cytometry. (B) Correlation between GFP and mApple expression at steady-state in cell lines stably expressing ATF4 reporter. (C) uORF1,2(ATF4)-mApple expression normalized to promoter and translational activity (mEGFP) in Δ IGHMBP2 K562 reporter cell lines at steady-state in DMSO or treated with 250 nM thapsigargin overnight. (D) Relative mApple/mEGFP intensities among reporter cell lines expressing BFP, BFP-IGHMBP2 or IGHMBP2-BFP, which were (E) gated for all BFP+ cells.

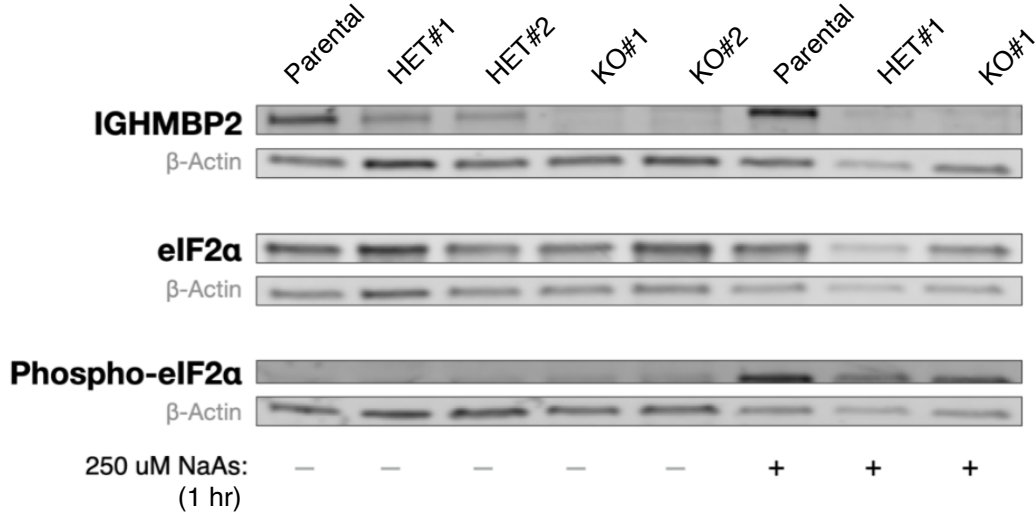
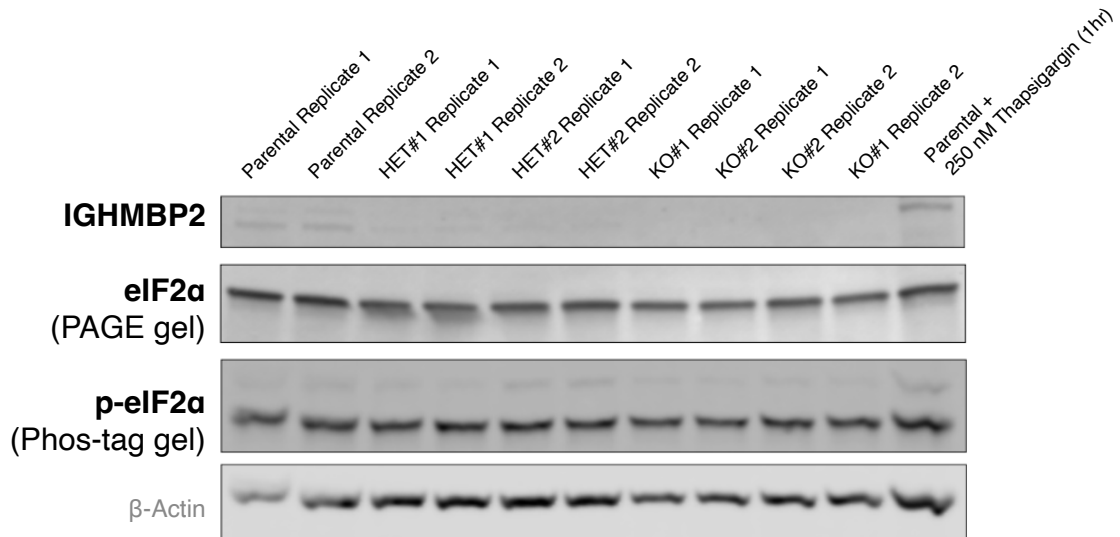
A**B**

Figure S9. Differential p-eIF2α levels at steady-state in IGHMBP2 deletion clones is not detected by Western blot.

(A) Western blots using PAGE with 50 μg total protein per lane and (B) Phos-Tag gels loaded with 20 μg total protein from Parental, HET Clone #1, HET Clone #2, KO Clone #1, and KO Clone #2 clones. B also shows a corresponding control PAGE gel run in parallel to confirm p-eIF2α Phos-tag gel shifts are not attributed to degradation. Both A and B were incubated with anti-eIF2α Ab, while a separate western blot in A was incubated with anti-p-eIF2α(S51) Ab.

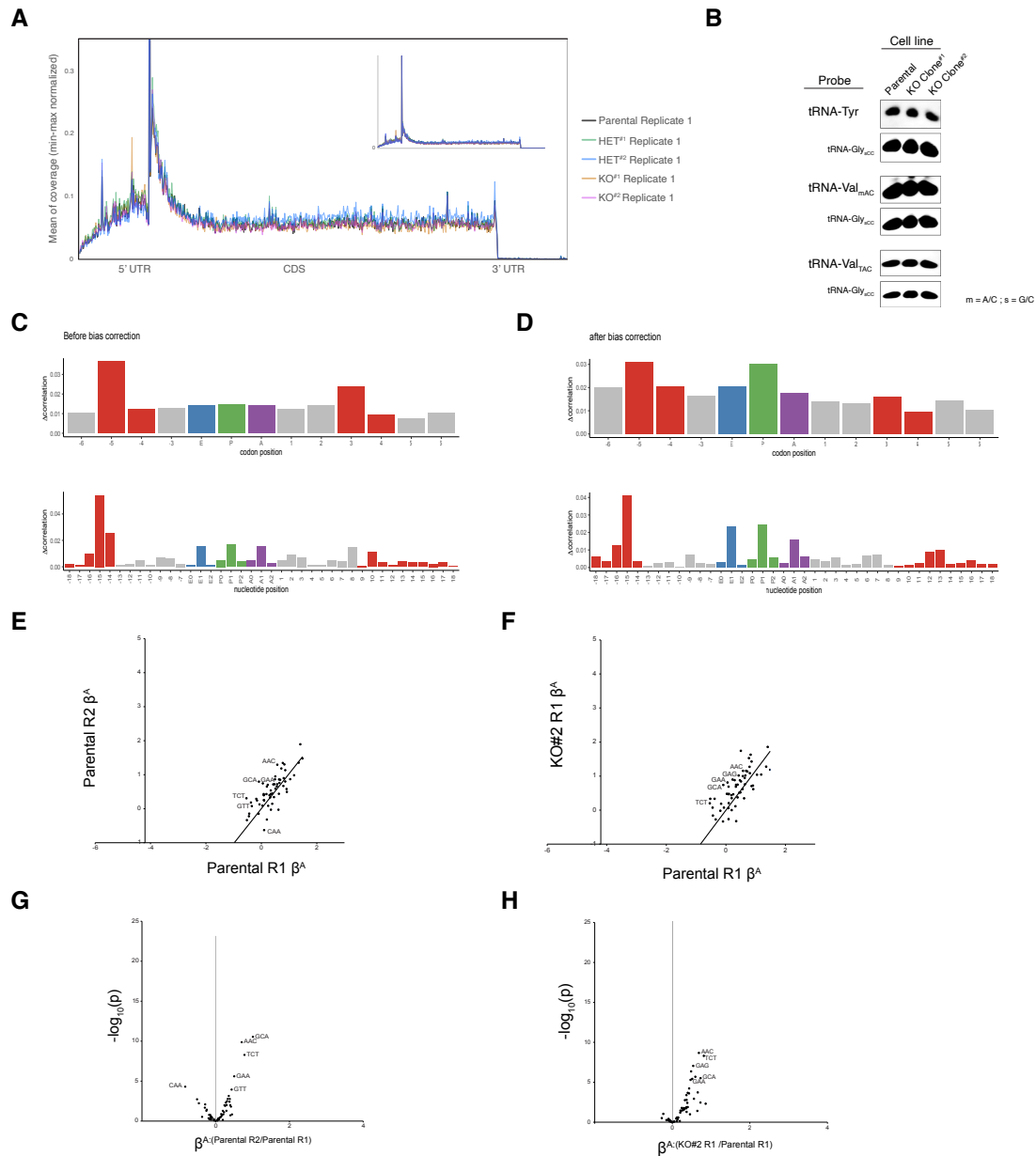


Figure S10. Ribosome footprint analyses across transcript regions and codons.

(A) Representative metagenome analysis for one replicate per Parental, HET Clone #1, HET Clone #2, KO Clone #1, and KO Clone #2 clones. Zoom-out view capturing the entire TSS peak is shown in the panel. (B) Northern blot visualizing tRNA-Tyr (all isodecoders), tRNA-Val_{mAC} (GUU/C/G isodecoders), tRNA-Val_{TAC} (GUA isodecoders), and tRNA-Gly_{scc} (GGC/U/G isodecoders) abundances in K562 cell lines with differential IGHMBP2 expression. 5 μ g total RNA was loaded per lane per gel. (C-D) Representative before and after footprint position bias-correction for one replicate of Parental Ribo-seq sample processed with *choros*. (E-F) A-site codon regression coefficients between parental replicates and KO Clone #2 relative to a parental sample, respectively. (G-H) Differential A-site codon enrichment analysis visualized by regression coefficient interaction terms between parental replicates and KO Clone #2 relative to a parental sample, respectively. E and G are shown to illustrate expected noise among reference and experimental comparisons.

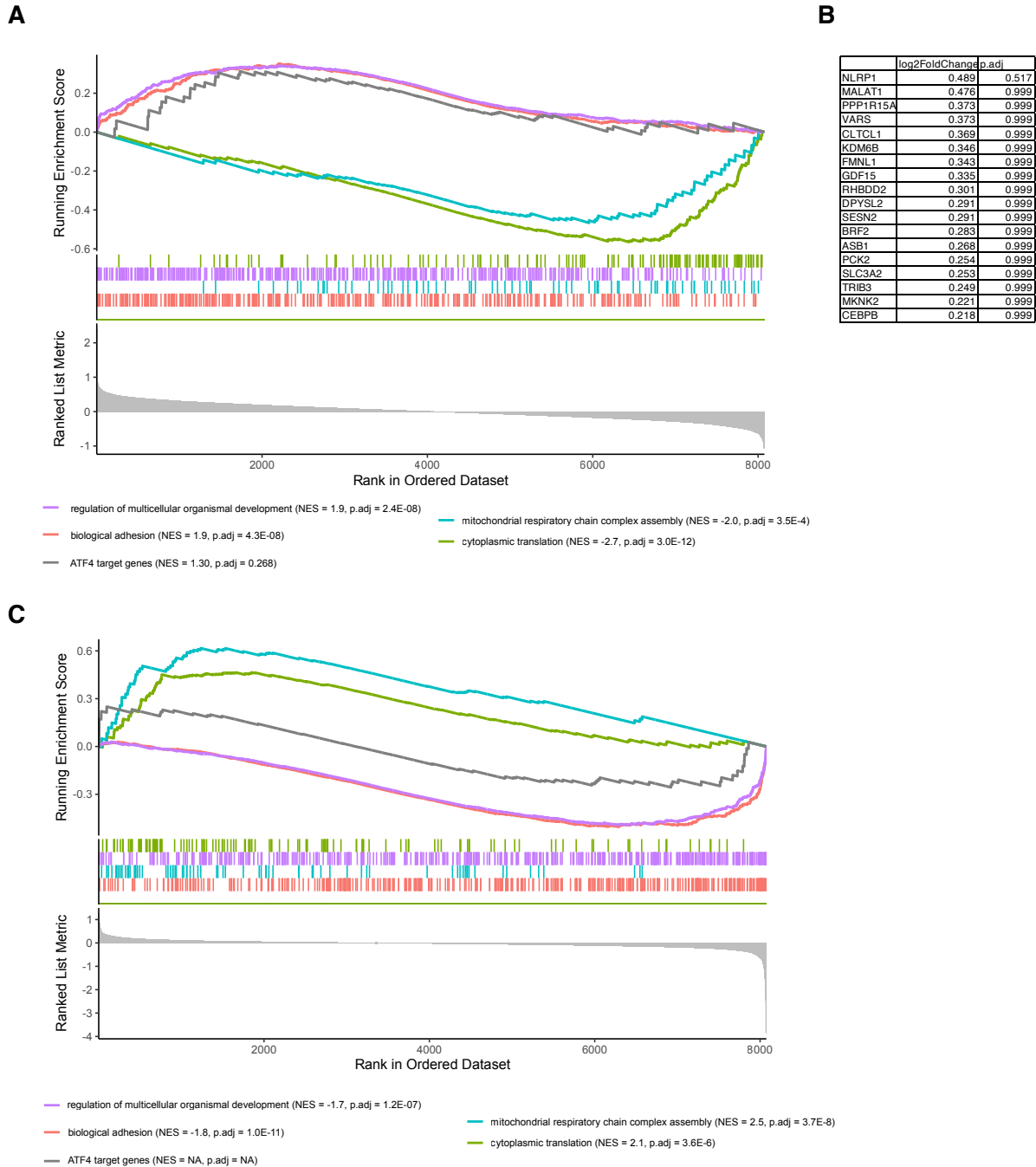


Figure S11. GSEA with ATF4 target gene list.

(A) Rank-gene profile of ATF4 target gene list among TE DEGs from IGHMBP2 KO clones, with representative significant gene sets shown for comparison. (B) Gene set list result from ATF4 target GSE in TE DEGs from IGHMBP2 KO clones, with average L2FC between KO clones #1 and #2 and p-adjusted values per gene shown. (C) Rank-gene profile of ATF4 target gene list among RNA-seq DEGs from IGHMBP2 KO clones, with representative significant gene sets shown for comparison. GSEA was computed using the Biological Processes ontology; min GS size = 25, max GS size = 1,000 with 100,000 permutations.

TABLES

Supplemental Table A. Prelim. functional assessment of IGHMBP2 mutagenesis

Supplemental Table A. (Preliminary) is a .pdf file uploaded to Supplemental files.

Supplemental Table 1. RNA-seq and Ribo-seq DEG results lists.

Supplemental Table 1 is an .xlsx file uploaded to Supplemental files.

Supplemental Table 2. RNA-seq and Ribo-seq GSEA results lists.

Supplemental Table 2 is an .xlsx file uploaded to Supplemental files.

References

- Banchs I, Casasnovas C, Albertí A, Jorge LD, Povedano M, Montero J, Martínez-Matos JA, Volpini V. 2009. Diagnosis of Charcot-Marie-Tooth Disease. *J Biomed Biotechnol* **2009**: 985415.
- Bohnsack KE, Yi S, Venus S, Jankowsky E, Bohnsack MT. 2023. Cellular functions of eukaryotic RNA helicases and their links to human diseases. *Nat Rev Mol Cell Biol* **24**: 749–769.
- Calviello L, Venkataramanan S, Rogowski KJ, Wyler E, Wilkins K, Tejura M, Thai B, Krol J, Filipowicz W, Landthaler M, et al. 2021. DDX3 depletion represses translation of mRNAs with complex 5' UTRs. *Nucleic Acids Res* **49**: gkab287-.
- Chen NN, Kerr D, Chang C-F, Honjo T, Khalili K. 1997. Evidence for regulation of transcription and replication of the human neurotropic virus JCV genome by the human Subp-2 protein in glial cells. *Gene* **185**: 55–62.
- Chothani S, Adami E, Ouyang JF, Viswanathan S, Hubner N, Cook SA, Schafer S, Rackham OJL. 2019. deltaTE: Detection of Translationally Regulated Genes by Integrative Analysis of Ribo-seq and RNA-seq Data. *Curr Protoc Mol Biology* **129**: e108.
- Cook SA, Johnson KR, Bronson RT, Davisson MT. 1995. Neuromuscular degeneration (nmd): a mutation on mouse Chromosome 19 that causes motor neuron degeneration. *Mamm Genome* **6**: 187–191.
- Costa-Mattioli M, Walter P. 2020. The integrated stress response: From mechanism to disease. *Science* **368**.
- Cottenie E, Kochanski A, Jordanova A, Bansagi B, Zimon M, Horga A, Jaunmuktane Z, Saveri P, Rasic VM, Baets J, et al. 2014. Truncating and Missense Mutations in IGHMBP2 Cause Charcot-Marie Tooth Disease Type 2. *Am J Hum Genetics* **95**: 590–601.
- Cox GA, Mahaffey CL, Frankel WN. 1998. Identification of the Mouse Neuromuscular Degeneration Gene and Mapping of a Second Site Suppressor Allele. *Neuron* **21**: 1327–1337.

- Dittmar KA, Goodenbour JM, Pan T. 2006. Tissue-Specific Differences in Human Transfer RNA Expression. *PLoS Genet* **2**: e221.
- Fukita Y, Mizuta TR, Shirozu M, Ozawa K, Shimizu A, Honjo T. 1993. The human S mu bp-2, a DNA-binding protein specific to the single-stranded guanine-rich sequence related to the immunoglobulin mu chain switch region. *J Biol Chem* **268**: 17463–17470.
- Gadek M, Sherr EH, Floor SN. 2023. The variant landscape and function of DDX3X in cancer and neurodevelopmental disorders. *Trends Mol Med* **29**: 726–739.
- Giannini A, Pinto AM, Rossetti G, Prandi E, Tiziano D, Brahe C, Nardocci N. 2006. Respiratory failure in infants due to spinal muscular atrophy with respiratory distress type 1. *Intensiv Care Med* **32**: 1851–1855.
- Gilbert LA, Horlbeck MA, Adamson B, Villalta JE, Chen Y, Whitehead EH, Guimaraes C, Panning B, Ploegh HL, Bassik MC, et al. 2014. Genome-Scale CRISPR-Mediated Control of Gene Repression and Activation. *Cell* **159**: 647–661.
- Grohmann K, Schuelke M, Diers A, Hoffmann K, Lucke B, Adams C, Bertini E, Leonhardt-Horti H, Muntoni F, Ouvrier R, et al. 2001. Mutations in the gene encoding immunoglobulin μ -binding protein 2 cause spinal muscular atrophy with respiratory distress type 1. *Nat Genet* **29**: 75–77.
- Grohmann K, Rossoll W, Kobsar I, Holtmann B, Jablonka S, Wessig C, Stoltenburg-Didinger G, Fischer U, Hübner C, Martini R, et al. 2004. Characterization of Ighmbp2 in motor neurons and implications for the pathomechanism in a mouse model of human spinal muscular atrophy with respiratory distress type 1 (SMARD1). *Hum Mol Genet* **13**: 2031–2042.
- Guan B-J, Hoef V van, Jobava R, Elroy-Stein O, Valasek LS, Cargnello M, Gao X-H, Krokowski D, Merrick WC, Kimball SR, et al. 2017. A Unique ISR Program Determines Cellular Responses to Chronic Stress. *Mol Cell* **68**: 885-900.e6.
- Guenther U-P, Handoko L, Lagerbauer B, Jablonka S, Chari A, Alzheimer M, Ohmer J, Plöttner O, Gehring N, Sickmann A, et al. 2009a. IGHMBP2 is a ribosome-associated helicase inactive in the neuromuscular disorder distal SMA type 1 (DSMA1). *Hum Mol Genet* **18**: 1288–1300.

- Guenther U-P, Handoko L, Varon R, Stephani U, Tsao C-Y, Mendell JR, Lützkendorf S, Hübner C, Au K von, Jablonka S, et al. 2009b. Clinical variability in distal spinal muscular atrophy type 1 (DSMA1): determination of steady-state IGHMBP2 protein levels in five patients with infantile and juvenile disease. *J Mol Medicine* **87**: 31–41.
- Harding HP, Novoa I, Zhang Y, Zeng H, Wek R, Schapira M, Ron D. 2000. Regulated Translation Initiation Controls Stress-Induced Gene Expression in Mammalian Cells. *Mol Cell* **6**: 1099–1108.
- Hart T, Chandrashekar M, Aregger M, Steinhart Z, Brown KR, MacLeod G, Mis M, Zimmermann M, Fradet-Turcotte A, Sun S, et al. 2015. High-Resolution CRISPR Screens Reveal Fitness Genes and Genotype-Specific Cancer Liabilities. *Cell* **163**: 1515–1526.
- Inglis, A. J., Masson, G. R., Shao, S., Perisic, O., McLaughlin, S. H., Hegde, R. S., & Williams, R. L. 2019. Activation of GCN2 by the ribosomal P-stalk. *Proceedings of the National Academy of Sciences*, *116*: 4946-4954.
- Ishimura, R., Nagy, G., Dotu, I., Chuang, J. H., & Ackerman, S. L. 2016. Activation of GCN2 kinase by ribosome stalling links translation elongation with translation initiation. *Elife* **5**: e14295.
- Joseph S, Robb SA, Mohammed S, Lillis S, Simonds A, Manzur AY, Walter S, Wraige E. 2009. Interfamilial phenotypic heterogeneity in SMARD1. *Neuromuscul Disord* **19**: 193–195.
- Kanaan J, Raj S, Decourty L, Saveanu C, Croquette V, Hir HL. 2018. UPF1-like helicase grip on nucleic acids dictates processivity. *Nat Commun* **9**: 3752.
- Kerr D, Khalili K. 1991. A recombinant cDNA derived from human brain encodes a DNA binding protein that stimulates transcription of the human neurotropic virus JCV. *J Biol Chem* **266**: 15876–15881.
- Korotkevich, G., Sukhov, V., Budin, N., Shpak, B., Artyomov, M. N., & Sergushichev, A. 2016. Fast gene set enrichment analysis. *bioRxiv*, 060012.
- Lee JW, Beebe K, Nangle LA, Jang J, Longo-Guess CM, Cook SA, Davisson MT, Sundberg JP, Schimmel P, Ackerman SL. 2006. Editing-defective tRNA

- synthetase causes protein misfolding and neurodegeneration. *Nature* **443**: 50–55.
- Lei L, Zhiqiang L, Xiaobo L, Zhengmao H, Shunxiang H, Huadong Z, Beisha T, Ruxu Z. 2022. Clinical and genetic features of Charcot-Marie-Tooth disease patients with IGHMBP2 mutations. *Neuromuscul Disord* **32**: 564–571.
- Lim SC, Bowler MW, Lai TF, Song H. 2012. The Ighmbp2 helicase structure reveals the molecular basis for disease-causing mutations in DMSA1. *Nucleic Acids Res* **40**: 11009–11022.
- Love, M.I., Huber, W., Anders, S. 2014. Moderated estimation of fold change and dispersion for RNA-seq data with DESeq2. *Genome Biology* **15**:550.
- Lu PD, Harding HP, Ron D. 2004. Translation reinitiation at alternative open reading frames regulates gene expression in an integrated stress response. *J Cell Biol* **167**: 27–33.
- Martin PB, Holbrook SE, Hicks AN, Hines TJ, Bogdanik LP, Burgess RW, Cox GA. 2022. Clinically relevant mouse models of Charcot–Marie–Tooth type 2S. *Hum Mol Genet*.
- Maystadt I, Zarhrate M, Landrieu P, Boespflug-Tanguy O, Sukno S, Collignon P, Melki J, Verellen-Dumoulin C, Munnich A, Viollet L. 2004. Allelic heterogeneity of SMARD1 at the IGHMBP2 locus. *Hum Mutat* **23**: 525–526.
- Mercuri E, Pera MC, Scoto M, Finkel R, Muntoni F. 2020. Spinal muscular atrophy – insights and challenges in the treatment era. *Nat Rev Neurol* **16**: 706–715.
- Messina MF, Messina S, Gaeta M, Rodolico C, Damiano AMS, Lombardo F, Crisafulli G, Luca FD. 2012. Infantile spinal muscular atrophy with respiratory distress type I (SMARD 1): An atypical phenotype and review of the literature. *Eur J Paediatr Neurol* **16**: 90–94.
- Mizuta T-R, Fukita Y, Miyoshi T, Shimizu A, Honjo T. 1993. Isolation of cDNA encoding a binding protein specific to 5'-phosphorylated single-stranded DNA with G-rich sequences. *Nucleic Acids Res* **21**: 1761–1766.

- Mok A, Tunney R, Benegas G, Wallace EWJ, Lareau LF. 2023. choros: correction of sequence-based biases for accurate quantification of ribosome profiling data. *bioRxiv* 2023.02.21.529452.
- Nakamura A, Nambu T, Ebara S, Hasegawa Y, Toyoshima K, Tsuchiya Y, Tomita D, Fujimoto J, Kurasawa O, Takahara C, et al. 2018. Inhibition of GCN2 sensitizes ASNS-low cancer cells to asparaginase by disrupting the amino acid response. *Proc Natl Acad Sci* **115**: E7776–E7785.
- Neill G, Masson GR. 2023. A stay of execution: ATF4 regulation and potential outcomes for the integrated stress response. *Front Mol Neurosci* **16**.
- Novoa I, Zhang Y, Zeng H, Jungreis R, Harding HP, Ron D. 2003. Stress-induced gene expression requires programmed recovery from translational repression. *EMBO J* **22**: 1180–1187.
- Pattali, R., Mou, Y. & Li, XJ. AAV9 Vector: a Novel modality in gene therapy for spinal muscular atrophy. 2019. *Gene Ther* **26**: 287–295.
- Pierson TM, Tart G, Adams D, Toro C, Golas G, Tiffit C, Gahl W. 2011. Infantile-onset spinal muscular atrophy with respiratory distress-1 diagnosed in a 20-year-old man. *Neuromuscul Disord* **21**: 353–355.
- Planell-Saguer M de, Schroeder DG, Rodicio MC, Cox GA, Mourelatos Z. 2009. Biochemical and genetic evidence for a role of IGHMBP2 in the translational machinery. *Hum Mol Genet* **18**: 2115–2126.
- Rudnik-Schöneborn S, Forkert R, Hahnen E, Wirth B, Zerres K. 1996. Clinical spectrum and diagnostic criteria of infantile spinal muscular atrophy: further delineation on the basis of SMN gene deletion findings. *Neuropediatrics* **27**:8–15
- Rzepnikowska W, Kocharński A. 2021. Models for IGHMBP2-Associated Diseases: An Overview and a Roadmap for the Future. *Neuromuscular Disord* **31**: 1266–1278.
- Saladini M, Nizzardo M, Govoni A, Taiana M, Bresolin N, Comi GP, Corti S. 2020. Spinal muscular atrophy with respiratory distress type 1: Clinical phenotypes, molecular pathogenesis and therapeutic insights. *J Cell Mol Med* **24**: 1169–1178.
- Scheper GC, Knaap MS van der, Proud CG. 2007. Translation matters: protein synthesis defects in inherited disease. *Nat Rev Genet* **8**: 711–723.

- Shababi, M., Feng, Z., Villalon, E., Sibigroth, C.M., Osman, E.Y., Miller, M.R., Williams-Simon, P.A., Lombardi, A., Sass, T.H., Atkinson, A.K. et al. 2016. Rescue of a mouse model of spinal muscular atrophy with respiratory distress type 1 (SMARD1) by AAV9-IGHMBP2 is dose dependent. *Mol. Ther* **24**: 855–866.
- Sheu-Gruttadauria J, Yan X, Stuurman N, Floor SN, Vale RD. 2023. Nucleolar dynamics are determined by the ordered assembly of the ribosome. *bioRxiv* 2023.09.26.559432.
- Simone C, Nizzardo M, Rizzo F, Ruggieri M, Riboldi G, Salani S, Bucchia M, Bresolin N, Comi GP, Corti S. 2014. iPSC-Derived Neural Stem Cells Act via Kinase Inhibition to Exert Neuroprotective Effects in Spinal Muscular Atrophy with Respiratory Distress Type 1. *Stem Cell Rep* **3**: 297–311.
- Skre H. 1974. Genetic and clinical aspects of Charcot-Marie-Tooth's disease. *Clin Genet* **6**: 98–118.
- Spaulding EL, Hines TJ, Bais P, Tadenev ALD, Schneider R, Jewett D, Pattavina B, Pratt SL, Morelli KH, Stum MG, et al. 2021. The integrated stress response contributes to tRNA synthetase-associated peripheral neuropathy. *Science* **373**: 1156–1161.
- Stavnezer J, Guikema JEJ, Schrader CE. 2008. Mechanism and Regulation of Class Switch Recombination. *Annu Rev Immunol* **26**: 261–292.
- Sugarman EA, Nagan N, Zhu H, Akmaev VR, Zhou Z, Rohlfes EM, Flynn K, Hendrickson BC, Scholl T, Sirko-Osadsa DA, et al. 2012. Pan-ethnic carrier screening and prenatal diagnosis for spinal muscular atrophy: clinical laboratory analysis of >72 400 specimens. *Eur J Hum Genet* **20**: 27–32.
- Sun Y, Eshov A, Zhou J, Isiktas AU, Guo JU. 2020. C9orf72 arginine-rich dipeptide repeats inhibit UPF1-mediated RNA decay via translational repression. *Nat Commun* **11**: 3354.
- Surrey V, Zöller C, Lork AA, Moradi M, Balk S, Dombert B, Saal-Bauernschubert L, Briese M, Appenzeller S, Fischer U, et al. 2018. Impaired Local Translation of β -actin mRNA in Ighmbp2-Deficient Motoneurons: Implications for Spinal Muscular Atrophy with respiratory Distress (SMARD1). *Neuroscience* **386**: 24–40.

- Taiana M, Govoni A, Salani S, Kleinschmidt N, Galli N, Saladini M, Ghezzi SB, Melzi V, Bersani M, Bo RD, et al. 2022. Molecular analysis of SMARD1 patient-derived cells demonstrates that nonsense-mediated mRNA decay is impaired. *J Neurol, Neurosurg Psychiatry* **93**: 908–910.
- Umate P, Tuteja N, Tuteja R. 2010. Genome-wide comprehensive analysis of human helicases. *Commun Integr Biol* **4**: 118–37.
- Vattem KM, Wek RC. 2004. Reinitiation involving upstream ORFs regulates ATF4 mRNA translation in mammalian cells. *Proc Natl Acad Sci* **101**: 11269–11274.
- Vadla GP, Hernandez SMR, Mao J, Garro-Kacher MO, Lorson ZC, Rice RP, Hansen SA, Lorson CL, Singh K, Lorson MA. 2022. ABT1 modifies SMARD1 pathology via interactions with IGHMBP2 and stimulation of ATPase and helicase activity. *JCI Insight* **8**: e164608.
- Wu T, Hu E, Xu S, Chen M, Guo P, Dai Z, Feng T, Zhou L, Tang W, Zhan L, Fu x, Liu S, Bo X, Yu G. 2021. clusterProfiler 4.0: A universal enrichment tool for interpreting omics data. *The Innovation*, **2**: 100141.
- Yu G, Wang L, Han Y, He. 2012. “clusterProfiler: an R package for comparing biological themes among gene clusters.” *OMICS: A Journal of Integrative Biology*, **16**: 284-287.
- Yuan J-H, Hashiguchi A, Yoshimura A, Yaguchi H, Tsuzaki K, Ikeda A, Wada-Isoe K, Ando M, Nakamura T, Higuchi Y, et al. 2017. Clinical diversity caused by novel IGHMBP2 variants. *J Hum Genet* **62**: 599–604.
- Zuko A, Mallik M, Thompson R, Spaulding EL, Wienand AR, Been M, Tadenev ALD, Bakel N van, Sijlmans C, Santos LA, et al. 2021. tRNA overexpression rescues peripheral neuropathy caused by mutations in tRNA synthetase. *Science* **373**: 1161–1166.

Publishing Agreement

It is the policy of the University to encourage open access and broad distribution of all theses, dissertations, and manuscripts. The Graduate Division will facilitate the distribution of UCSF theses, dissertations, and manuscripts to the UCSF Library for open access and distribution. UCSF will make such theses, dissertations, and manuscripts accessible to the public and will take reasonable steps to preserve these works in perpetuity.

I hereby grant the non-exclusive, perpetual right to The Regents of the University of California to reproduce, publicly display, distribute, preserve, and publish copies of my thesis, dissertation, or manuscript in any form or media, now existing or later derived, including access online for teaching, research, and public service purposes.

DocuSigned by:

Jesslyn Park

E90150C16960401...

Author Signature

12/14/2023

Date